

Quark masses using twisted-mass fermion gauge ensembles

C. Alexandrou,^{1,2} S. Bacchio,² G. Bergner,³ M. Constantinou,⁴ M. Di Carlo,^{5,6} P. Dimopoulos,⁷ J. Finkenrath,² E. Fiorenza,⁸ R. Frezzotti,⁹ M. Garofalo,¹⁰ K. Hadjiyiannakou,^{1,2} B. Kostrzewa,¹¹ G. Koutsou,² K. Jansen,¹² V. Lubicz,¹³ M. Mangin-Brinet,¹⁴ F. Manigrasso,^{1,9,15} G. Martinelli,¹⁶ E. Papadiofantous,^{1,2} F. Pittler,² G. C. Rossi,^{9,17} F. Sanfilippo,¹⁸ S. Simula,¹⁸ C. Tarantino,¹³ A. Todaro,^{1,9,15} C. Urbach,¹⁰ and U. Wenger¹⁹

(Extended Twisted Mass Collaboration)

¹*Department of Physics, University of Cyprus, 20537 Nicosia, Cyprus*

²*Computation-based Science and Technology Research Center, The Cyprus Institute, 20 Konstantinou Kavafi Street, 2121 Nicosia, Cyprus*

³*University of Jena, Institute for Theoretical Physics, Max-Wien-Platz 1, D-07743 Jena, Germany*

⁴*Department of Physics, Temple University, Philadelphia, Pennsylvania 19122–1801, USA*

⁵*School of Physics and Astronomy, The University of Edinburgh, Edinburgh EH9 3FD, United Kingdom*

⁶*Istituto Nazionale di Fisica Nucleare, Sezione di Roma La Sapienza, Piazzale Aldo Moro 5, I-00185 Roma, Italy*

⁷*Dipartimento di Scienze Matematiche, Fisiche e Informatiche, Università di Parma and INFN, Gruppo Collegato di Parma, Parco Area delle Scienze 7/a (Campus), 43124 Parma, Italy*

⁸*CP³-Origins, University of Southern Denmark, Campusvej 55, 5230 Odense, Denmark*

⁹*Dipartimento di Fisica and INFN, Università di Roma “Tor Vergata”, Via della Ricerca Scientifica 1, I-00133 Roma, Italy*

¹⁰*HISKP (Theory), Rheinische Friedrich-Wilhelms-Universität Bonn, Nussallee 14-16, 53115 Bonn, Germany*

¹¹*High Performance Computing and Analytics Lab, Rheinische Friedrich-Wilhelms-Universität Bonn, Friedrich-Hirzebruch-Allee 8, 53115 Bonn, Germany*

¹²*NIC, DESY, Platanenallee 6, D-15738 Zeuthen, Germany*

¹³*Dipartimento di Matematica e Fisica, Università Roma Tre and INFN, Sezione di Roma Tre, Via della Vasca Navale 84, I-00146 Rome, Italy*

¹⁴*Theory Group, Laboratoire de Physique Subatomique et de Cosmologie, CNRS/IN2P3 38026 Grenoble, France*

¹⁵*Institut für Physik, Humboldt-Universität zu Berlin, Newtonstrasse 15, 12489 Berlin, Germany*

¹⁶*Dipartimento di Fisica and INFN, Università di Roma “La Sapienza”, Piazzale Aldo Moro 5, I-00185 Roma, Italy*

¹⁷*Centro Fermi, Museo Storico della Fisica e Centro Studi e Ricerche “Enrico Fermi”, Piazza del Viminale 1, I-00184 Roma, Italy*

¹⁸*Istituto Nazionale di Fisica Nucleare, Sezione di Roma Tre, Via della Vasca Navale 84, I-00146 Rome, Italy*

¹⁹*Institute for Theoretical Physics, Albert Einstein Center for Fundamental Physics, University of Bern, Sidlerstrasse 5, CH-3012 Bern, Switzerland*



(Received 5 May 2021; accepted 15 September 2021; published 19 October 2021)

We present a calculation of the up, down, strange, and charm quark masses performed within the lattice QCD framework. We use the twisted-mass fermion action and carry out simulations that include in the sea two light mass-degenerate quarks, as well as the strange and charm quarks. In the analysis, we use gauge ensembles simulated at three values of the lattice spacing and with light quarks that correspond to pion masses in the range from 350 MeV to the physical value, while the strange and charm quark masses are tuned approximately to their physical values. We use several quantities to set the scale in order to check for finite lattice spacing effects, and in the continuum limit, we get compatible results. The quark mass renormalization is carried out nonperturbatively using the (modified) Regularization Independent Momentum Subtraction (RI'-MOM) method converted into the $\overline{\text{MS}}$ scheme. For the determination of

Published by the American Physical Society under the terms of the [Creative Commons Attribution 4.0 International](#) license. Further distribution of this work must maintain attribution to the author(s) and the published article's title, journal citation, and DOI. Funded by SCOAP³.

the quark masses, we use physical observables from both the meson and the baryon sectors, obtaining $m_{ud} = 3.636(66)(^{+60}_{-57})$ MeV and $m_s = 98.7(2.4)(^{+4.0}_{-3.2})$ MeV in the $\overline{\text{MS}}(2 \text{ GeV})$ scheme and $m_c = 1036(17)(^{+15}_{-8})$ MeV in the $\overline{\text{MS}}(3 \text{ GeV})$ scheme, where the first errors are statistical and the second ones are combinations of systematic errors. For the quark mass ratios, we get $m_s/m_{ud} = 27.17(32)(^{+56}_{-38})$ and $m_c/m_s = 11.48(12)(^{+25}_{-19})$.

DOI: [10.1103/PhysRevD.104.074515](https://doi.org/10.1103/PhysRevD.104.074515)

I. INTRODUCTION

Quark masses are essential inputs of the Standard Model (SM) and play a primary role for the description of a large number of physical processes that can provide insights into the dynamics of the SM as well as in the search of beyond the Standard Model physics. The quark masses together with the strong coupling constant can be regarded as the fundamental parameters of QCD, the renormalizable theory of the strong interactions. Therefore, their determination plays a crucial role in the phenomenological description of the plethora of complex phenomena governed by strong nuclear forces taking place in the Universe as well as at particle colliders. Lattice QCD provides a nonperturbative approach based on first principles and systematically improvable for determining the quark masses and the strong coupling. In this approach, the QCD Lagrangian is defined on a discrete Euclidean four-dimensional space-time lattice of large but finite extent, which allows for numerical simulation of the theory via Monte Carlo methods. The finite volume and the nonvanishing lattice spacing introduce systematic artifacts, which can be theoretically understood, kept under numerical control, and extrapolated away in order to extract the physical quantities of interest.

Theoretical progress in lattice field theory and improvement in numerical algorithms, accompanied with a continuously increasing computational power, are allowing us to perform simulations using physical values of the light-quark masses. However, most of these simulations are still carried out using a single lattice spacing and volume, although this is rapidly changing as more lattice QCD collaborations gain access to larger computational resources and can produce multiple ensembles of gauge configurations generated with physical values of the light quark masses. Such ensembles will be referred to as physical point ensembles. In this work, we include two physical point ensembles at two different lattice spacings. In order to take the continuum limit, we also employ additional ensembles at a coarser lattice resolution with larger than physical pion masses. Globally, we thus use ensembles with three values of the lattice spacing and spanning pion masses in the range from about 350 to 135 MeV, which enable us to perform a combined chiral and continuum extrapolation. In order to study systematic effects in the determination of the quark masses, we use two sets of observables to set the scale and to evaluate the quark masses. One set of observables is based on quantities from the meson sector of QCD, while the other set relies on

baryonic observables. In the former case, we use the pion mass and decay constant to set the scale and to determine the average up/down quark mass. The mass of the strange and charm quarks are extracted using the kaon and D -meson masses, respectively. In the latter case, instead, the masses of the pion and nucleon are employed to set the scale and fix the average up/down quark mass, while the Ω^- and the Λ_c masses determine the strange and charm quark masses, respectively. In this way, we obtain a valuable consistency check with respect to the results coming from the mesonic sector.

For the renormalization of the quark mass, we employ a dedicated set of gauge ensembles with four mass-degenerate sea quarks (having mass around half of the strange quark mass). Such a set ensures a good control of the extrapolation to the massless limit. We perform the computation in an intermediate mass-independent scheme, which is finally converted to the standard $\overline{\text{MS}}$ scheme.

The paper is organized as follows. In Sec. II, we describe the gauge ensembles used in this study and explain our methodology. In Secs. III and IV, we present the methods used to set the lattice spacing a and to carry out a nonperturbative computation of the renormalization constant Z_P including a detailed discussion on the control of hadronic contaminations and other systematic errors. In Secs. V and VI, we describe the extraction of the quark masses and their ratios using inputs from the mesonic and baryonic sectors, respectively. In Sec. VII, we discuss our final results and give our conclusions and outlook.

II. METHODOLOGY

In twisted-mass lattice QCD [1], the discretized Dirac operator in the *physical* quark basis is written as

$$D(\mu_f) = \frac{1}{2}\gamma_\mu(\nabla_\mu + \nabla_\mu^*) - i\gamma_5\left\{m_{\text{cr}}(r_f) - r_f\frac{a}{2}\nabla_\mu\nabla_\mu^* + \frac{c_{\text{SW}}(r_f)}{32}\gamma_\mu\gamma_\nu(Q_{\mu\nu} - Q_{\nu\mu})\right\} + \mu_f, \quad (1)$$

where $r_f = \pm 1$, ∇_μ and ∇_μ^* are nearest-neighbor forward and backward covariant derivatives, μ_f sets the mass of the quark field q_f of flavor f , c_{SW} is the coefficient of the clover-term $Q_{\mu\nu}$ [2], and m_{cr} is the critical value of the “untwisted” mass m_0 , obtained by requiring the vanishing of the partially conserved *axial* current (PCAC) mass, as

discussed in Ref. [3]. This condition, referred to as maximal twist, guarantees automatic $\mathcal{O}(a)$ improvement of physical observables [4,5]. In the twisted-mass fermion formulation at maximal twist, the renormalized quark masses are thus given by

$$m_f = \frac{\mu_f}{Z_P} = \frac{(a\mu_f)}{aZ_P}, \quad (2)$$

where a is the lattice spacing and Z_P is the pseudoscalar renormalization constant. Therefore, the determination of both Z_P and the lattice spacing, combined with inputs from known physical quantities depending on the quark masses, enables us to extract m_f . Having gauge ensembles with at least three different lattice spacings at several pion masses allows us to take the continuum limit, and by performing a chiral extrapolation, we can determine the quark masses at the physical point.

A. Gauge ensembles

We use the twisted-mass fermion discretization scheme [1,4] with the inclusion of a clover term [2]. As already explained, twisted-mass fermions (TMFs) provide an attractive formulation for lattice QCD simulations allowing for automatic $\mathcal{O}(a)$ improvement of physical observables as well as renormalization constants [4,6]. This is an important property since quantities of interest have lattice artifacts of $\mathcal{O}(a^2)$ and are thus closer to the continuum limit. A clover term is added to the TMF action to suppress

$\mathcal{O}(a^2)$ breaking effects between the neutral and charged pions, which eventually leads to the stabilization of simulations with light quark masses close to the physical pion mass. For more details on the TMF formulation, see Refs. [7,8], and on the simulation and tuning strategies, see Refs. [9,10].

In this study, we analyze ten gauge ensembles simulated at three values of the lattice spacing and at several values of the pion mass, spanning a range from the physical pion mass up to 350 MeV. Some parameters of these ensembles and the values of few key physical quantities are listed in Table I. More details are given in Ref. [11]. With respect to Ref. [11], the ensemble cC211.20.48 has been added in order to investigate the light quark mass dependence at the finest lattice spacing.

The ensembles are generated with two mass-degenerate light quarks and the strange and charm quarks in the sea ($N_f = 2 + 1 + 1$ ensembles). The strange and charm sea quark mass parameters, $a\mu_\sigma$ and $a\mu_\delta$ (see, e.g., Eq. (8) of Ref. [12]) have been adjusted so as to reproduce the phenomenological conditions $m_c/m_s \simeq 11.8$ and $m_{D_s}/f_{D_s} \simeq 7.9$ [13], which are easy to implement with few percent level precision even using simulations with larger than physical pion masses and on lattices of linear size $L \simeq 2.5$ fm, as detailed in Ref. [10]. The condition on m_{D_s}/f_{D_s} is sensitive to the charm quark mass, while the one on m_c/m_s fixes the strange quark mass. In this way, the charm and strange sea quark mass parameters have been tuned, separately for each lattice resolution (or β), to bare values that *a posteriori* turn out to yield values for the renormalized sea quark masses that

TABLE I. Parameters of the $N_f = 2 + 1 + 1$ ensembles analyzed in this study. In the first column, we give the name of the ensemble; in the second, we give the lattice volume; in the third, we give the number of molecular dynamics units simulated per ensemble; in the fourth, we give the twisted-mass parameter, $a\mu_\ell$, for the average up/down (light) quark; in the fifth and in the sixth, we give the pion mass am_π and decay constant af_π in lattice units from Ref. [11]; in the seventh, we give the pion mass times the lattice spatial length, $m_\pi L$; in the eighth, we give the ratio m_N/m_π as determined in Sec. VI; and, finally, in the last column, we give the pion mass in physical units, using our determination of the gradient-flow scale w_0 obtained in Ref. [11] [see later Eq. (32)]. We also include for each set of ensembles with the same lattice spacing the coupling constant β , the clover-term parameter c_{SW} , the parameters of the nondegenerate operator $a\mu_\sigma$ and $a\mu_\delta$, related to the renormalized strange and charm sea quark masses [5], and the value of the gradient-flow scale w_0/a determined at the physical pion mass in Ref. [11].

Ensemble	$L^3 \times T$	MDUs	$a\mu_\ell$	am_π	af_π	$m_\pi L$	m_N/m_π	m_π (MeV)
$\beta = 1.726, c_{SW} = 1.74, a\mu_\sigma = 0.1408, a\mu_\delta = 0.1521, w_0/a = 1.8352(35)$								
cA211.53.24	$24^3 \times 48$	5026	0.00530	0.16626 (51)	0.07106 (36)	3.99	...	346.4 (1.6)
cA211.40.24	$24^3 \times 48$	5298	0.00400	0.14477 (70)	0.06809 (30)	3.47	...	301.6 (2.1)
cA211.30.32	$32^3 \times 64$	10234	0.00300	0.12530 (16)	0.06674 (15)	4.01	4.049 (14)	261.1 (1.1)
cA211.12.48	$48^3 \times 96$	2936	0.00120	0.08022 (18)	0.06133 (33)	3.85	5.685 (28)	167.1 (0.8)
$\beta = 1.778, c_{SW} = 1.69, a\mu_\sigma = 0.1246864, a\mu_\delta = 0.1315052, w_0/a = 2.1299(16)$								
cB211.25.32	$32^3 \times 64$	3959	0.00250	0.10475 (45)	0.05652 (38)	3.35	4.104 (36)	253.3 (1.4)
cB211.25.48	$48^3 \times 96$	5246	0.00250	0.10465 (14)	0.05726 (12)	5.02	4.124 (17)	253.0 (1.0)
cB211.14.64	$64^3 \times 128$	6187	0.00140	0.07848 (10)	0.05477 (12)	5.02	5.119 (36)	189.8 (0.7)
cB211.072.64	$64^3 \times 128$	3161	0.00072	0.05659 (8)	0.05267 (14)	3.62	6.760 (30)	136.8 (0.6)
$\beta = 1.836, c_{SW} = 1.6452, a\mu_\sigma = 0.106586, a\mu_\delta = 0.107146, w_0/a = 2.5045(17)$								
cC211.20.48	$48^3 \times 96$	2000	0.00200	0.08540 (17)	0.04892 (13)	4.13	4.244 (25)	245.73 (98)
cC211.06.80	$80^3 \times 160$	3207	0.00060	0.04720 (7)	0.04504 (10)	3.78	6.916 (19)	134.3 (0.5)

are consistent within statistical errors of few percents with those we determine in this paper, as discussed in the following, at the physical pion mass point, on large volumes and in the continuum limit.

B. Osterwalder-Seiler fermions

A naive use of the twisted-mass action for nondegenerate strange and charm quarks would lead to an undesired $O(a^2)$ mixing of the strange and charm flavors in the correlation functions of interest to determine physical quantities [14,15]. In order to avoid such a mixing in the correlation functions, we adopt a nonunitary lattice setup [5] where the twisted-mass action for nondegenerate strange and charm quarks is employed only in the sea sector, while the valence strange and charm quarks that enter the correlation functions are regularized as exactly flavor-diagonal Osterwalder-Seiler fermions [16]. Thus, the valence action in the strange and charm sectors ($f = s, c$) reads

$$S_{OS}^f(\mu_f) = a^4 \sum_x \bar{q}_f(x) D(\mu_f) q_f(x), \quad (3)$$

where $D(\mu_f)$ is the twisted-mass Dirac operator in Eq. (1) with the same values of m_0 and c_{SW} as in the sea sector action used for ensemble generations. As the renormalized strange and charm sea quark masses are matched with few percent relative accuracy to their valence counterparts, no significant unitarity violation is expected in our continuum limit results.

When constructing meson correlation functions, the Wilson parameters of the two valence quarks are always chosen to have opposite values. This choice guarantees that squared pseudoscalar meson masses, generically indicated by m_{PS}^2 , differ from their continuum counterparts only by terms of order $\mathcal{O}(a^2\mu)$ [4,7]. As we said above, in our lattice setup, the (valence) flavor conservation is guaranteed in all correlation functions, and automatic $\mathcal{O}(a)$ improvement is maintained. Of course, we need to fix the valence strange and charm quark masses, μ_s and μ_c , by imposing suitable renormalization conditions. For this purpose, in the present work, we use two different sets of observables. Namely, in one case, we use the mass of the physical masses of kaon and D (or D_s) mesons, and in the other case, we use the masses of the Ω and Λ_c baryons. These two different choices will lead to two different determinations of the strange and charm quark masses, which will enable us to check the consistency of our results when using physical inputs from the mesonic and baryonic sectors.

III. SCALE SETTING

As already mentioned, we have ensembles at three different lattice spacings. We will refer to the ensembles in Table I that start with cA in their names as A ensembles, those starting with cB as B ensembles, and those with cC as

TABLE II. The values of the lattice spacing extracted from the pion sector (second row) and using the nucleon mass (third row) for the A, B, and C ensembles, denoted by a_A , a_B , and a_C , respectively. In the last row, we show the difference Δa between the lattice spacings determined using the nucleon mass and from the pion sector.

Sector	a_A (fm)	a_B (fm)	a_C (fm)
Pion	0.09471(39)	0.08161(30)	0.06942(26)
Nucleon	0.09295(47)	0.07975(32)	0.06860(20)
Δa	0.00176(61)	0.00186(44)	0.00082(32)

C ensembles (the label c stands for *clover*). Each of these groups has the same lattice spacing, with the A ensembles having the largest lattice spacing and C ensembles having the smallest one. In what follows, we will use different quantities to determine the three lattice spacings. This will allow us to check consistency while taking the continuum limit when different inputs are used. In the pion sector, the pion mass and decay constant are used as input. Within this approach, one also determines the value of the gradient-flow scale w_0 . We use the isosymmetric values of the pion mass and decay constant, given, respectively, by [17]

$$m_\pi^{\text{isoQCD}} = 135.0(2) \text{ MeV} \quad \text{and} \quad f_\pi^{\text{isoQCD}} = 130.4(2) \text{ MeV}. \quad (4)$$

We also compute the value of w_0/a for each ensemble (see Table I) and extrapolate to the physical pion mass and continuum limit. We find $w_0 = 0.17383(63) \text{ fm}$ [11], and using this value, one determines the lattice spacings shown in Table II. We refer to this determination of the lattice spacings as coming from the “pion” sector. Details are given in Ref. [11].

Another quantity used for the determination of the lattice spacings is the mass of the nucleon [18,19]. Details on the extraction of the nucleon mass are given in Sec. VI. In order to fit the pion mass dependence of the nucleon mass, we use the well established SU(2) chiral perturbation theory result to one loop [20,21],

$$m_N(m_\pi) = m_N^0 - 4c_1 m_\pi^2 - \frac{3g_A^2}{16\pi f_\pi^2} m_\pi^3. \quad (5)$$

The three values of the lattice spacing, which will be denoted by a_A , a_B , and a_C , can be determined from the lattice data for the nucleon and pion masses by rewriting Eq. (5) as

$$(a_i m_N) = a_i m_N^0 - 4c_1 \frac{(a_i m_\pi)^2}{a_i} - \frac{3g_A^2}{16\pi f_\pi^2} \frac{(a_i m_\pi)^3}{a_i^2}, \quad (6)$$

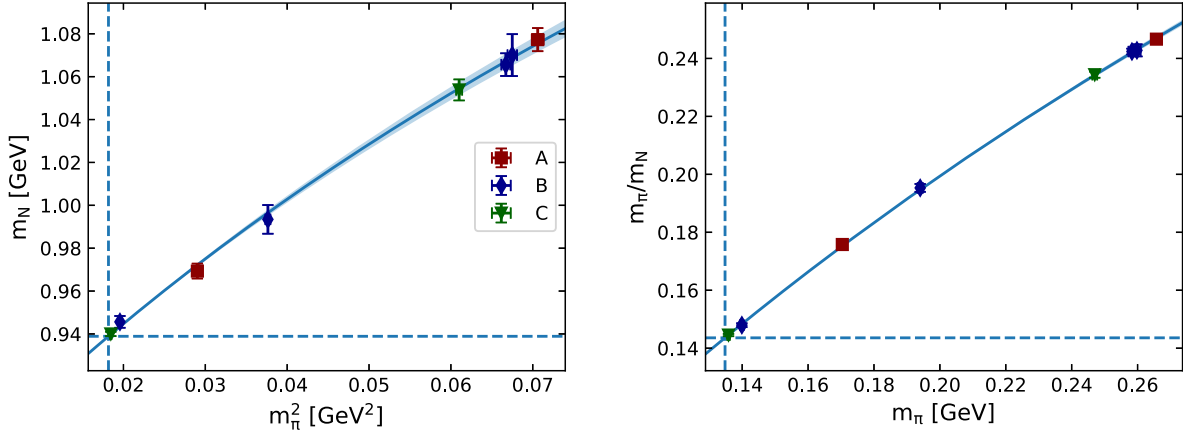


FIG. 1. Determination of the lattice spacing from the nucleon mass. In the left panel, we show the nucleon mass as a function of the pion mass m_π squared. In the right panel, we show the dimensionless quantity m_π/m_N as a function of m_π , using the lattice spacing extracted from the nucleon mass. The values of m_π/m_N are listed in Table I, while am_N and am_π are determined in Sec. VI. The solid line shows the fit to the lattice QCD data using Eq. (5). The value of $\chi^2/\text{d.o.f.}$ is 0.19, where the number of degrees of freedom is 5.

where $(a_i m_N)$ and $(a_i m_\pi)$ are our lattice QCD results and $i = A, B, C$. The three quantities a_i as well as the nucleon mass in the chiral limit, m_N^0 , are treated as fitting parameters, while the value of c_1 is fixed by requiring the reproduction of the physical value of the nucleon mass, m_N^{isoQCD} , at the physical pion point (4), namely,

$$c_1 = \left[m_N^0 - \frac{3g_A^2}{16\pi f_\pi^2} (m_\pi^{\text{isoQCD}})^3 - m_N^{\text{isoQCD}} \right] / [4(m_\pi^{\text{isoQCD}})^2]. \quad (7)$$

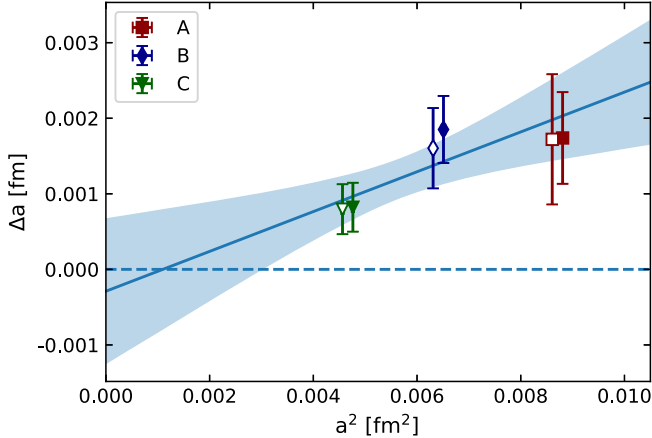


FIG. 2. The difference Δa between the lattice spacings determined from the pion sector and the nucleon mass versus a^2 . Full symbols are the lattice spacings determined using all the ensembles for which $m_\pi < 260$ MeV. Open symbols, shifted to the left for clarity, are obtained using ensembles for which the pion mass is below 190 MeV. The solid line shows the linear fit in a^2 to the results extracted by using ensembles with $m_\pi < 260$ MeV (full symbols), which is largely consistent with zero in the continuum limit.

We restrict ourselves to using ensembles for which the pion mass is below 260 MeV since chiral perturbation theory to higher orders has larger ambiguities. The simulations of the gauge ensembles use mass-degenerate up and down quarks and include no electromagnetic effects. Thus, we use the average value of the proton and neutron mass as our input for fixing the lattice spacings; namely, we assume $m_N^{\text{isoQCD}} = 0.9389$ GeV in Eq. (7). We also use the physical value for the axial charge, $g_A = 1.27641(56)$ [22], and for consistency the physical value of f_π from Eq. (4). The ratio g_A/f_π appears in the m_π^3 term, and any residual correction due to strong isospin breaking and electromagnetism is neglected.

The result of the fit to the mass of the nucleon m_N is depicted in Fig. 1 and describes very well the data, yielding $\chi^2/\text{d.o.f.} = 0.19$, where d.o.f. are the number of degrees of freedom. We find $m_N^0 = 0.8737(14)$ GeV, $c_1 = -1.090(20)$ GeV $^{-1}$, and the values of the lattice spacings shown in the third row of Table II. In Fig. 1, we also show the ratio m_N/m_π and the resulting fit using the parameters extracted from the fit to the nucleon mass. As can be seen, the data for m_N/m_π are well described.

The values of the lattice spacing extracted from the pion sector and from the nucleon mass are shown in Table II, and they differ by $\mathcal{O}(a^2)$ effects. Fitting their difference as a function of a^2 is shown in Fig. 2. We observe that in the continuum limit the difference vanishes, as expected for our $\mathcal{O}(a)$ -improved formalism. In what follows, we will use both determinations to extract the quark masses. This provides a cross-check for our procedure and for the magnitude of any residual lattice spacing effect.

IV. COMPUTATION OF Z_P

In order to determine the renormalized quark masses, it is crucial to perform an accurate evaluation of the mass

TABLE III. Parameters for the $N_f = 4$ ensembles used for the calculation of Z_P . By am_{PS} , we denote the pseudoscalar (nonsinglet) meson mass, and by am_{PCAC} , we denote the PCAC untwisted mass (see Ref. [3]), both given in lattice units. Note that on all the $N_f = 4$ ensembles, taking into account statistical errors, the values of am_{PCAC} are typically 15 to 100 times smaller than the lowest twisted-mass values.

$\beta = 1.726 \ 24^3 \times 48$			$\beta = 1.778 \ 24^3 \times 48$			$\beta = 1.836 \ 32^3 \times 64$		
$a\mu_{\text{sea}}$	am_{PS}	am_{PCAC}	$a\mu_{\text{sea}}$	am_{PS}	am_{PCAC}	$a\mu_{\text{sea}}$	am_{PS}	am_{PCAC}
0.0060	0.1689(15)	$-4.1(1.4) \times 10^{-4}$	0.0075	0.1748(15)	$-2.3(0.8) \times 10^{-5}$	0.0050	0.1276(14)	$-4.3(3.1) \times 10^{-5}$
0.0080	0.1905(11)	$-4.3(1.1) \times 10^{-5}$	0.0088	0.1871(18)	$-8.6(8.0) \times 10^{-5}$	0.0065	0.1447(14)	$+5.9(2.1) \times 10^{-5}$
0.0100	0.2155(12)	$+1.5(1.3) \times 10^{-4}$	0.0100	0.2006(18)	$-1.6(0.8) \times 10^{-4}$	0.0080	0.1585(14)	$+1.6(0.3) \times 10^{-4}$
0.0115	0.2289(12)	$+1.7(1.1) \times 10^{-4}$	0.0115	0.2158(11)	$+0.2(9.5) \times 10^{-5}$	0.0095	0.1744(12)	$+2.0(0.3) \times 10^{-4}$

renormalization factor Z_m , that in the maximally twisted-mass formulation is given by $Z_m = 1/Z_P$ [see Eq. (2)]. For this reason, the details of the procedure we have followed to compute Z_P will be given in this section.

For the calculation of Z_P , we employ the nonperturbative RI'-MOM renormalization scheme [23], which is a mass-independent scheme since the renormalization constants are defined in the massless limit. The choice of this intermediate scheme is convenient in that the scale evolution for the renormalization constants of the operators with nontrivial anomalous dimension is controlled by the renormalized gauge coupling alone. This requires, however, simulations close enough to the chiral limit, which is not the case of the $N_f = 2 + 1 + 1$ ensembles of Table I, mainly due to the presence of the heavy sea charm quark. In order to safely take the chiral limit in the computation of the renormalization constants, we have thus separately produced gauge field configurations with four mass-degenerate quarks ($N_f = 4$) at the same value of the coupling β and with the same clover term included in the fermionic action as for our A, B, and C ensembles of Table I. This ensures that in the chiral limit the same massless $N_f = 4$ QCD theory underlies both the ensembles used for computing hadronic observables and setting the energy scale (see Table I) and the ensembles dedicated to the evaluation of the renormalization constants, about which details are given in Table III. The four degenerate quarks are taken with masses from approximately 8 to 16 times larger than the average up-down quark mass, which simplifies both the simulations and the tuning to maximal twist. The values of the critical mass m_{cr} have been chosen in order to satisfy the maximal twist condition (which is convenient to reduce lattice artifacts) to a very good accuracy level, as can be deduced from the smallness of the PCAC masses in Table III (actually, the tuning is even slightly better than the one corresponding to the $N_f = 2 + 1 + 1$ ensembles of Table I).

In the RI'-MOM scheme, we obtain the renormalization constant of the (flavor nonsinglet) pseudoscalar density

operator $O_P = i\bar{q}\gamma_5 q$ with $r'_q = -r_q = -1$ and $\mu_{q'} = \mu_q$ via the following condition,¹

$$Z_q^{-1} Z_P \frac{1}{12} \text{Tr}[\gamma^5 \mathcal{V}_P(p)]|_{p^2=\mu_0^2} = 1, \quad (8)$$

where \mathcal{V}_P is the pseudoscalar vertex function between quark and antiquark states with momentum p and Z_q is the renormalization constant of the quark field, defined as

$$Z_q = -\frac{i}{12} \text{Tr} \left[\frac{\not{p}}{p^2} S_q^{-1}(p) \right] \Big|_{p^2=\mu_0^2}. \quad (9)$$

Here, S_q is the quark propagator at momentum p , which is identified with the renormalization scale μ_0 . In this work, we adopt the alternative definition of Z_q first proposed in Ref. [6],

$$Z_q = -\frac{i}{12N_p} \sum_{\mu}' \text{Tr} \left[\frac{\gamma_{\mu}}{\tilde{p}_{\mu}} S_q^{-1}(p) \right] \Big|_{p^2=\mu_0^2}, \quad (10)$$

where the sum \sum' is over the N_p nonvanishing components of the lattice momentum $a\tilde{p}_{\mu} = \sin(ap_{\mu})$. The prescription of Eq. (10), unlike the naive RI'-MOM definition (9), has no lattice artifacts at tree level, and beyond tree level, it exhibits quite small $\mathcal{O}(a^2)$ cutoff effects.

The subtraction of the Goldstone pole in the vertex function \mathcal{V}_P requires good control of the vertex mass dependence. Therefore, we find it more suitable to adopt a partially quenched (PQ) setup, in which propagators and vertices are computed for multiple values of valence quark masses μ_{val} at fixed sea mass μ_{sea} ; namely, we use

¹The relevant fermionic action density is $\bar{q}D(\mu_q)q + \bar{q}'D(\mu_{q'})q' = \bar{X}[\gamma_{\nu}(\nabla + \nabla^*)_{\nu}/2 + (m_{cr}(1) - a/2\nabla_{\nu}^*\nabla_{\nu}) + i\gamma_5\tau^3\mu_q + (c_{sw}(1)/32)\gamma_{\mu}\gamma_{\nu}(Q_{\mu\nu} - Q_{\nu\mu})]X$, where $X = (\chi_q, \chi_{q'})^T$ is a valence quark field pair in the canonical quark basis for standard Wilson fermions (after which, as usual, the renormalization constants are named) and $q = \exp(i\gamma_5\pi/4)\chi_q$, $q' = \exp(-i\gamma_5\pi/4)\chi_{q'}$, $\bar{q} = \bar{\chi}_q \exp(i\gamma_5\pi/4)$, and $\bar{q}' = \bar{\chi}_{q'} \exp(-i\gamma_5\pi/4)$. Note in particular that $i\bar{q}\gamma_5 q' = i\bar{\chi}_q\gamma_5\chi_{q'}$.

$$\begin{aligned}
a\mu_{\text{val}}^A &= \{0.0060, 0.0080, 0.0100, 0.0115, 0.0130, 0.0150, 0.0170, 0.0190, 0.0210\}, \\
a\mu_{\text{val}}^B &= \{0.0050, 0.0060, 0.0075, 0.0090, 0.0100, 0.0110, 0.0130, 0.0150, 0.0170\}, \\
a\mu_{\text{val}}^C &= \{0.0040, 0.0050, 0.0065, 0.0080, 0.0095, 0.0110, 0.0125, 0.0140, 0.0155\}.
\end{aligned} \tag{11}$$

The chiral extrapolation of the pseudoscalar vertex is discussed in details in Sec. IV B below.

For each ensemble, we employ a large number of momenta $ap = 2\pi(\frac{n_x}{L}, \frac{n_y}{L}, \frac{n_z}{L})$, in the range $(ap)^2 \in [0.24, 6.69]$ for the $24^3 \times 48$ ensembles and $(ap)^2 \in [0.13, 5.23]$ for the $32^3 \times 64$ ensembles. Quark propagators and vertices in momentum space are evaluated using $N_{\text{cfg}} = 200$ gauge configurations. In order to reduce the effect of Lorentz noninvariant cutoff effects, we filter the momenta selecting the ones that are isotropic (“democratic”) in the spatial directions, thus satisfying

$$\frac{\sum_{\mu} \tilde{p}_{\mu}^4}{(\sum_{\mu} \tilde{p}_{\mu}^2)^2} < 0.28. \tag{12}$$

The above constraint ensures that unwanted hypercubic lattice artifacts are suppressed [6]. We further improve the Z_P estimator by using results from lattice perturbation theory (for more details see, e.g., Refs. [24,25]). In summary, we calculate the lattice artifacts at one-loop level and to all orders in the lattice spacing, $\mathcal{O}(g^2 a^\infty)$. The perturbative corrections to the Green’s function of the pseudoscalar operator, as well as to the quark propagator, are evaluated for each momentum ap at which the renormalization constants are computed. It should be noted that each value of ap requires a separate calculation of the $\mathcal{O}(g^2 a^\infty)$ correction, as the perturbative contributions are not analytical and require the numerical evaluation of one-loop integrals. Such contributions also include the leading-order terms, $\mathcal{O}(g^2 a^0)$, that have to be separated from the pure $\mathcal{O}(a^n)$ terms ($n \neq 0$). The computation of perturbative lattice artifacts to $\mathcal{O}(g^2 a^\infty)$ done in Ref. [25] is adapted for the case of the specific definition of Z_q in Eq. (10). Thus, the one-loop perturbative corrections that we use are defined as

$$\Delta Z_q^{(1)}(ap) = Z_q^{(1)}(\log(ap), ap) - Z_q^{(1)}(\log(ap), 0), \tag{13}$$

$$\Delta \mathcal{V}_P^{(1)}(ap) = \mathcal{V}_P^{(1)}(\log(ap), ap) - \mathcal{V}_P^{(1)}(\log(ap), 0), \tag{14}$$

where $Z_q^{(1)}$ and $\mathcal{V}_P^{(1)}$ are the one-loop contributions to the quark field renormalization constant and to the pseudoscalar vertex, respectively.

Using the above quantities, we extract improved non-perturbative estimates for Z_q and Z_P by modifying the renormalization conditions as

$$Z_q^{\text{impr}} = Z_q - g^2 \Delta Z_q^{(1)}(a\mu_0), \tag{15}$$

$$(Z_q^{\text{impr}})^{-1} Z_P^{\text{impr}} \frac{1}{12} \text{Tr}[\gamma^5 (\mathcal{V}_P - g^2 \Delta \mathcal{V}_P^{(1)}(ap))] |_{p^2=\mu_0^2} = 1. \tag{16}$$

A. Analysis method and safety checks against hadronic contaminations

The improved Z_P estimators, namely, Z_P^{impr} obtained from Eq. (16), are evaluated at different values of $p^2 = \mu_0^2$ and extrapolated to the chiral limit, a step which is discussed in detail in the following Sec. IV B. Then, the chirally extrapolated lattice estimators of Z_P are evolved to a common reference scale $p^2 = \mu_{\text{ref}}^2$ in the RI'-MOM scheme using the anomalous dimension known up to next-to-next-to-next leading order (N³LO) according to Ref. [26] and adopting $\Lambda_{\text{QCD}}(N_f = 4) = 294(12)$ MeV from Ref. [13]. The curves obtained at the three β values are reported in Fig. 3 for two different values of the reference scale, namely, $\mu_{\text{ref}}^2 = 17$ GeV² and $\mu_{\text{ref}}^2 = 21$ GeV².

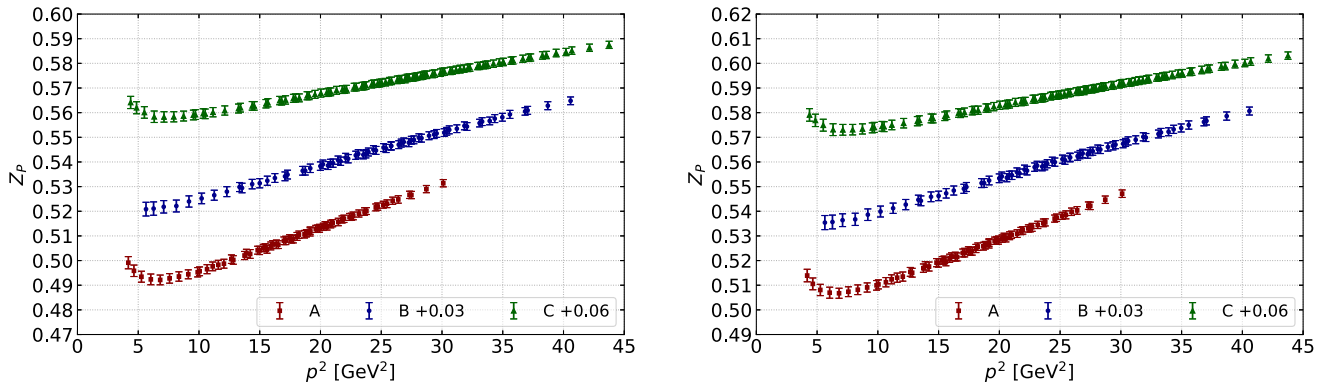


FIG. 3. Dependence of Z_P on the momentum p^2 for two values of the reference scale, $\mu_{\text{ref}}^2 = 17$ GeV² (left panel) and $\mu_{\text{ref}}^2 = 21$ GeV² (right panel). The vertical offsets shown in the inset are applied to the data of the corresponding ensembles.

TABLE IV. Results of the two fits on $Z_P(\mu_{\text{ref}}^2 = 17\text{GeV}^2)$, according to the fit ansatz in Eq. (17).

β	Ansatz	z_{-1}	z_0	z_1	z_2	$\chi^2/\text{d.o.f.}$
1.726	1		0.4762(28)	0.00190(23)	-0.00021(59)	0.4
	2	-0.011(43)	0.4782(52)	0.00178(13)		0.4
1.778	1		0.4828(39)	0.00117(25)	0.00053(56)	0.3
	2	0.033(42)	0.4772(40)	0.00147(10)		0.3
1.836	1		0.4888(29)	0.00101(19)	-0.00032(43)	0.03
	2	-0.021(30)	0.4922(34)	0.00083(08)		0.04

A dependence on p^2 of the $Z_P(\mu_{\text{ref}}^2)$ estimators in Fig. 3 is expected due to lattice artifacts, i.e., $\mathcal{O}(a^2 p^2)$ terms, and possibly also to residual $\mathcal{O}(a^0)$ hadronic contaminations,² which, however, must vanish as $1/p^2$ at large p^2 . The plots of $Z_P(\mu_{\text{ref}}^2)$ in Fig. 3 show very good linearity in p^2 within the range $p^2 \in [15, 24] \text{ GeV}^2$, which is the one relevant for our determination of Z_P and hence of the renormalized quark masses. This fact indicates that lattice artifacts other than $a^2 p^2$ -terms and possible hadronic contamination effects are negligible within our small statistical errors. Such a property is explicitly checked at each β value by performing a fit of $Z_P(\mu_{\text{ref}}^2 = 17 \text{ GeV}^2)$ (left panel of Fig. 3) with the two Ansätze given by

$$\begin{aligned} \text{Ansatz 1: } Z_P(\mu_{\text{ref}}^2) &= z_0 + z_1 p^2 + z_2 (p^2)^2, \\ \text{Ansatz 2: } Z_P(\mu_{\text{ref}}^2) &= z_0 + z_1 p^2 + \frac{z_{-1}}{p^2}. \end{aligned} \quad (17)$$

The resulting best fit values for z_i are given in Table IV. The coefficients z_2 and z_{-1} are compatible with zero within statistical errors at all β values, while the coefficients z_1 scale nicely with a^2 (see Table II). From this check, we see that the systematic uncertainties on Z_P are negligible within our small statistical errors. We will comment on the value of z_0 when we present our results in Sec. IV C.

Within the present study of renormalized quark masses, we follow two different methods for determining Z_P in the RI' scheme and use data in two different p^2 -ranges. The first method (M1) consists in fitting the $Z_P(\mu_{\text{ref}}^2)$ data linearly in p^2 in a given p^2 -range with the aim of removing $\mathcal{O}(a^2 p^2)$ discretization effects, while in the second method (M2), the same data are fitted to a constant [12]. Method M2 is by construction much less sensitive than M1 to possible small residual hadronic contaminations but at the expense of leaving some $\mathcal{O}(a^2)$ artifacts in the determination of Z_P . The ranges of p^2 used in the present analysis are $p^2 \in [15, 19] \text{ GeV}^2$ and $p^2 \in [18, 24] \text{ GeV}^2$ for determining $Z_P(17 \text{ GeV}^2)$ and $Z_P(21 \text{ GeV}^2)$, respectively.

As an additional check of our determination of $Z_P(\mu^2)$ in the RI'-MOM scheme, we show in Fig. 4 the results for the nonperturbative step scaling function

$\Sigma_P(\mu_A^2, \mu_B^2) = Z_P(\mu_A^2)/Z_P(\mu_B^2)$ versus $(a/w_0)^2$ for $(\mu_A^2, \mu_B^2) = (21.5, 14.3) \text{ GeV}^2$. We see that the lattice QCD data exhibit small discretization errors and agree in the continuum limit with the perturbative counterpart $\Sigma_P^{\text{pt}}(\mu_A^2, \mu_B^2) = 1.058$, which is computed to N³LO [26].

Moreover, as will be shown in Sec. V, using the four Z_P determinations corresponding to the methods M1 and M2 and at the two reference scales $\mu_{\text{ref}}^2 = 17 \text{ GeV}^2$ and $\mu_{\text{ref}} = 21 \text{ GeV}^2$, we obtain in the continuum limit consistent final results for the renormalized quark masses.

B. Chiral extrapolation and Goldstone boson pole subtraction

A crucial step in determining the renormalization constant Z_P is the extrapolation of its lattice estimators to the chiral limit, where the mass-independent RI'-MOM scheme is defined.

1. Hadronic contaminations in the pseudoscalar vertex

It is well known that the pseudoscalar vertex \mathcal{V}_P receives contributions at the nonperturbative level by hadronic contaminations whose leading term scales as approximately $(p^2 m_\pi^2)^{-1}$ [23]. Such a Goldstone boson pole has to be identified and subtracted from the data. In a unitary

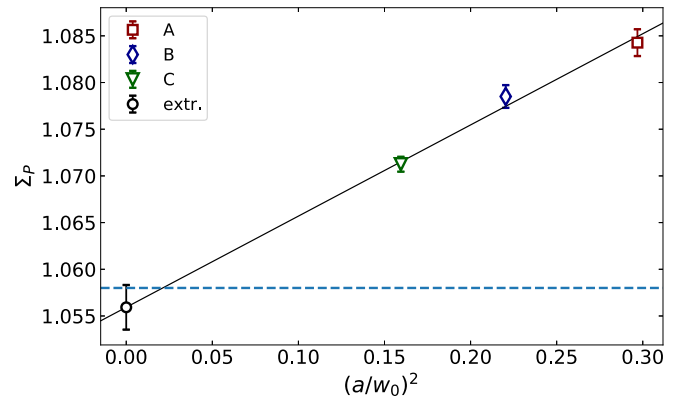


FIG. 4. The scaling function $\Sigma_P(\mu_A^2, \mu_B^2) = Z_P(\mu_A^2)/Z_P(\mu_B^2)$ vs $(a/w_0)^2$ for the three β -values studied (red square for $\beta = 1.726$, blue rhombus for $\beta = 1.778$, and green triangle for $\beta = 1.836$) as well as the continuum extrapolation (black circle). The dashed line shows the perturbative value, $\Sigma_P^{\text{pt}}(\mu_A^2, \mu_B^2) = 1.058$.

²This point is discussed, e.g., in the Appendix of Ref. [23].

lattice setup for QCD with $N_f = 4$ degenerate flavors of mass m_q , the lattice estimator of the vertex, $v_P(p^2, m_q)$, is expected to have the form

$$v_P(p^2, m_q) = \mathcal{V}_P(p^2) + h \frac{\Lambda_{\text{QCD}}^4}{p^2 m_\pi^2} + h' \frac{\Lambda_{\text{QCD}}^2}{p^2} + h'' m_q \frac{\Lambda_{\text{QCD}}}{p^2} + \dots, \quad (18)$$

where the dimensionless quantities \mathcal{V}_P (our target vertex), h , h' , and h'' depend in general on $a^2 p^2$, $a^2 \Lambda_{\text{QCD}}^2$, $a^2 m_q \Lambda_{\text{QCD}}$, and $a^2 m_q^2$, while the ellipses stand for terms suppressed by higher powers of $1/p^2$ as $p^2 \rightarrow \infty$. We note that terms linear in m_q are either hadronic contaminations suppressed as approximately $1/p^2$ at large p^2 or lattice artifacts of the form approximately $a^2 m_q \Lambda_{\text{QCD}}$, which are numerically tiny for the am_q values of interest here. Since close to the chiral limit $m_\pi^2 \sim m_q$, an equivalent Ansatz for $v_P(p^2, m_q)$ can be written in the form³

$$v_P(p^2, m_q) = \mathcal{V}_P(p^2) + \frac{1}{p^2} (\kappa m_q^{-1} + \kappa' + \kappa'' m_q) + \dots, \quad (19)$$

where we separate the hadronic contaminations decreasing, for large p^2 , like $1/p^2$ from the vertex of interest $\mathcal{V}_P(p^2)$.

2. Choice of a partially quenched setup

In a PQ setup, such as the one adopted in the present analysis (see Sec. IV A), the lattice action is power counting renormalizable, and the operator vertices evaluated at several values of valence (μ_{val}) and sea (μ_{sea}) quark masses approach, as $(\mu_{\text{val}}, \mu_{\text{sea}}) \rightarrow (0, 0)$, the corresponding unitary vertices from which the RI'-MOM renormalization constants can be computed. As detailed in Sec. IV A above, at all β values, we use nine values of μ_{val} for each of the four μ_{sea} values. This allows us to have a good control on the mass dependence of the pseudoscalar vertex and to adopt, at fixed β , p^2 , and μ_{sea} values, the following fit Ansatz for the chiral fit in μ_{val} ,

$$v_P(p^2, \mu_{\text{val}}, \mu_{\text{sea}}) = \mathcal{V}_P(p^2, \mu_{\text{sea}}) + H \frac{\Lambda_{\text{QCD}}^4}{p^2 [m_\pi^2]_{\text{val}}} + H' \frac{\Lambda_{\text{QCD}}^2}{p^2} + H'' \mu_{\text{val}} \frac{\Lambda_{\text{QCD}}}{p^2} + \dots, \quad (20)$$

where the quantities $\mathcal{V}_P(p^2, \mu_{\text{sea}})$, H , H' , and H'' depend, besides on μ_{sea} (to a numerically negligible level, as we shall see below), also on $a^2 p^2$, $a^2 \Lambda_{\text{QCD}}^2$, $a^2 m_q \Lambda_{\text{QCD}}$, and $a^2 m_q^2$, while the ellipses have the same meaning as in Eq. (18). Noting that the hadronic contaminations in the

three-point correlation function of quark, pseudoscalar bilinear, and antiquark fields at fixed 4-momenta (and in the derived quantity v_P) arise from the time orderings where the quark and antiquark fields are located at time distances both before or both after the pseudoscalar density [23], it follows that the Goldstone boson pole contamination is controlled by the mass $[m_\pi^2]_{\text{val}}$ of the valence pion that appears as an intermediate state in the aforementioned time orderings. Recalling also that, to leading order in PQ chiral perturbation theory, $[m_\pi^2]_{\text{val}} \sim \mu_{\text{val}}$ [27], we choose to use the equivalent Ansatz

$$v_P(p^2, \mu_{\text{val}}, \mu_{\text{sea}}) = \mathcal{V}_P(p^2, \mu_{\text{sea}}) + \frac{K}{p^2 \mu_{\text{val}}} + \frac{K'}{p^2} + \frac{K''}{p^2} \mu_{\text{val}} + \dots, \quad (21)$$

where again we separate the hadronic contaminations (suppressed like $1/p^2$ as $p^2 \rightarrow \infty$) from the vertex of interest and the dimensionful coefficients K , K' , and K'' in general depend on μ_{sea} and may be affected by lattice artifacts. From the fit of v_P in μ_{val} at fixed p^2 and μ_{sea} , one can determine the coefficients K and K'' , but it is not possible to disentangle the vertex $\mathcal{V}_P(p^2, \mu_{\text{sea}})$ from the hadronic contamination K'/p^2 . At this point, one can safely take the limit $\mu_{\text{sea}} \rightarrow 0$ and determine $\mathcal{V}_P(p^2, 0) + K'|_{\mu_{\text{sea}}=0}/p^2$. After taking the full chiral limit, one can check that the residual hadronic contamination $K'|_{\mu_{\text{sea}}=0}/p^2$ is completely negligible in the range of p^2 used for the extraction of Z_P , as already detailed in Sec. IV A (see the discussion around Table IV).

3. Numerical data and intermediate analysis results

Within the p^2 ranges used in the present analysis, our data for $v_P(p^2, \mu_{\text{val}}, \mu_{\text{sea}})$ exhibit a tiny linear dependence on μ_{val} , which is compatible with $K'' = \mathcal{O}(a^2)$ up to statistical errors. This is checked by fitting the data to the Ansatz of Eq. (21) for each fixed $a\mu_{\text{sea}}$ and p^2 , which

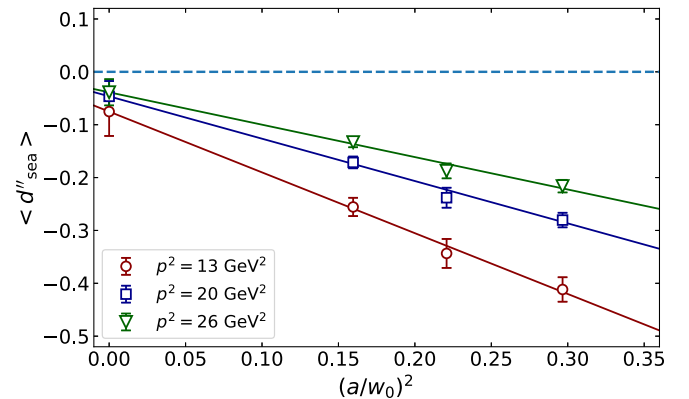


FIG. 5. Scaling of the coefficient $d'' \equiv K''/(w_0 p^2)$ averaged over μ_{sea} , $\langle d'' \rangle_{\text{sea}}$. The three curves correspond to different values of p^2 , namely, 13, 20, and 26 GeV^2 .

³Due to next-to-leading-order terms in the chiral expansion of m_π^2 , here κ' does not coincide with $h' \Lambda_{\text{QCD}}^2/p^2$.

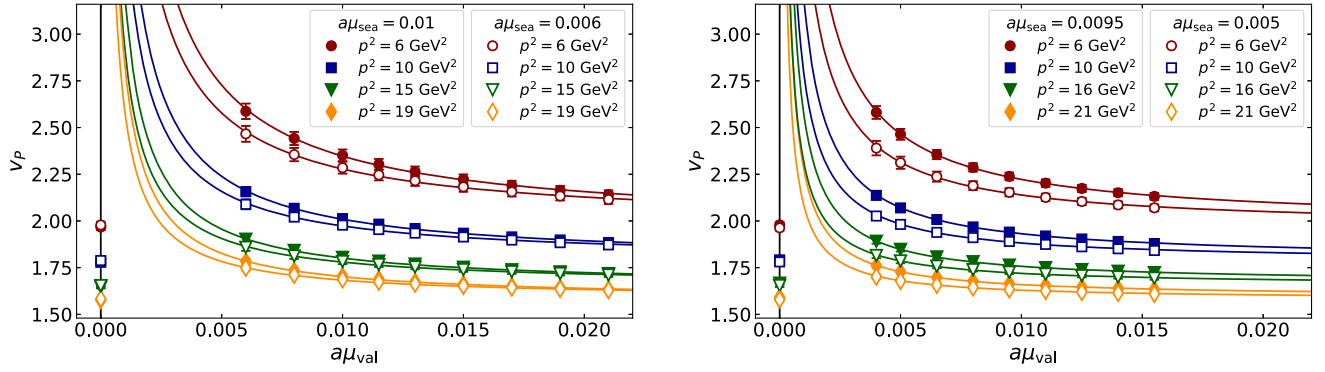


FIG. 6. Fit of the pseudoscalar vertex lattice estimators $v_P(p^2, \mu_{\text{val}}, \mu_{\text{sea}}; a)$ according to the Ansatz of Eq. (22) for $\beta = 1.726$ (left panel) and $\beta = 1.836$ (right panel). Different colors correspond to different values of p^2 , while full and empty circles correspond to different values of the sea quark mass $a\mu_{\text{sea}}$. The extrapolated values at $a\mu_{\text{val}} = 0$ correspond to the quantities $[\mathcal{V}_P(p^2, \mu_{\text{sea}}) + K'/p^2]$ in Eq. (22).

determines the quantities $[\mathcal{V}_P(p^2, \mu_{\text{sea}}) + K'/p^2]$, K/p^2 , and K''/p^2 , and then studying the dimensionless ratio $d'' \equiv K''/(w_0 p^2)$ as a function of $(a/w_0)^2$. At fixed β value, we observe that d'' changes with the sea quark mass of a given gauge ensemble nonmonotonically in μ_{sea} by the same amount as the statistical errors. Therefore, we average over the values of d'' at each μ_{sea} for a fixed β value, obtaining the quantity $\langle d'' \rangle_{\text{sea}}$, which is shown in Fig. 5 for three representative p^2 values, namely, 13, 20, and 26 GeV^2 . As one can see, the continuum limit of d'' is consistent with zero up to statistical errors and/or a small residual term, which, even if present (given the numerical values of $a\mu_{\text{val}} \lesssim 0.02$), would alter Z_P only to $\mathcal{O}(10^{-4})$. In view of the evidence that K'' is $\mathcal{O}(a^2)$ or numerically negligible in the p^2 range of interest here, we can perform the fit in μ_{val} on the data for v_P excluding the term linear in μ_{val} ; namely, we use

$$v_P(p^2, \mu_{\text{val}}, \mu_{\text{sea}}) = \left[\mathcal{V}_P(p^2, \mu_{\text{sea}}) + \frac{K'}{p^2} \right] + \frac{K}{p^2} \frac{1}{\mu_{\text{val}}}. \quad (22)$$

This procedure has the advantage of yielding small statistical errors at the price of including well-controlled $\mathcal{O}(a^2)$ artifacts in the numerical estimate of $[\mathcal{V}_P(p^2, \mu_{\text{sea}}) + K'/p^2]$ and hence of Z_P .

The results of the fit on v_P for few values of p^2 and the two extreme values of μ_{sea} are shown in Fig. 6 for the cases $\beta = 1.726$ and $\beta = 1.836$. Besides the very good quality of the fits, we remark that the resulting estimates of $[\mathcal{V}_P(p^2, \mu_{\text{sea}}) + K'/p^2]$ at $\mu_{\text{val}} = 0$ indeed show a very tiny dependence on μ_{sea} as mentioned above. Such a dependence on μ_{sea} turns out to be of the same size as the statistical errors (about 0.5%), nonmonotonic in μ_{sea} at fixed β and with different trends at different β 's.

This feature is illustrated in Fig. 7, where the resulting estimates of $Z_P(\mu_{\text{sea}}, p^2)$, obtained using the RI condition of Eq. (8), are shown at $\beta = 1.726$ and $\beta = 1.836$. Therefore, as the dependence on μ_{sea} of $Z_P(\mu_{\text{sea}}, p^2)$ is not statistically significant, we average them in order to estimate $Z_P(p^2)$ in the unitary chiral limit.

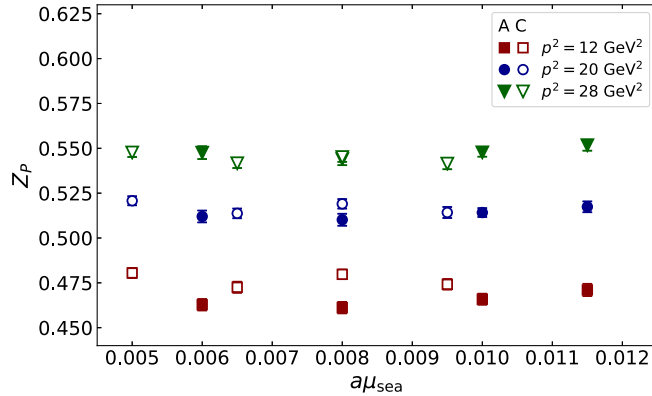


FIG. 7. Dependence of the renormalization constant $Z_P(\mu_{\text{sea}}, p^2)$ on the quark sea mass μ_{sea} at $\beta = 1.726$ (A) and $\beta = 1.836$ (C) for different values of the momentum $p^2 = (12, 20, 28) \text{ GeV}^2$.

TABLE V. Results for Z_P in RI'-MOM for each β value for methods M1 (second and fourth columns) and M2 (third and fifth columns), computed at reference scales of $\mu_{\text{ref}} = 17 \text{ GeV}^2$ (indicated by “a”) and $\mu_{\text{ref}} = 21 \text{ GeV}^2$ (indicated by “b”). For cases M1a and M2a, results are extracted in the range $p^2 \in (15, 19) \text{ GeV}^2$, while for M1b and M2b, $p^2 \in (18, 24) \text{ GeV}^2$.

β	RI'-MOM			
	M1a	M2a	M1b	M2b
1.726	0.4774(24)	0.5079(24)	0.4917(26)	0.5301(24)
1.778	0.4812(32)	0.5042(26)	0.4944(27)	0.5255(23)
1.836	0.4899(26)	0.5053(23)	0.5046(27)	0.5240(24)

TABLE VI. Results for Z_P in the RI'-MOM scheme but evolved to the common reference scale $\mu_{\text{ref}}^2 = 19 \text{ GeV}^2$. The notation is the same as that in Table V, and we report separately the statistical error and the systematic uncertainty related to the evolution factors.

RI'-MOM, $\mu_{\text{ref}}^2 = 19 \text{ GeV}^2$				
β	M1a	M2a	M1b	M2b
1.726	0.4849(24)(35)	0.5159(24)(37)	0.4851(26)(32)	0.5229(24)(34)
1.778	0.4888(33)(35)	0.5121(26)(37)	0.4877(27)(32)	0.5184(23)(34)
1.836	0.4976(26)(36)	0.5133(23)(37)	0.4978(27)(33)	0.5169(24)(34)

C. Results for Z_P in the RI'-MOM and $\overline{\text{MS}}$ schemes

In Table V, we give the results of Z_P determined in the RI'-MOM scheme using methods M1 and M2 (see Sec. IV A) for the two reference scales $\mu_{\text{ref}}^2 = 17 \text{ GeV}^2$ (labeled by “a”) and $\mu_{\text{ref}}^2 = 21 \text{ GeV}^2$ (labeled by “b”). We find that at each β value the parameter z_0 appearing in Eq. (17) is found to be compatible with the results for $Z_P(\mu_{\text{ref}}^2 = 17 \text{ GeV}^2)$ extracted using the method M1, as expected since this method corresponds to a linear fit Ansatz in p^2 . The results are obtained by fitting the data in the momentum ranges $p^2 \in (15, 19) \text{ GeV}^2$ and $p^2 \in (18, 24) \text{ GeV}^2$, respectively, for the reference scales 17 and 21 GeV^2 . The values of Z_P given in Table V (in the RI'-MOM scheme) are then evolved to the common reference scale $\mu_{\text{ref}}^2 = 19 \text{ GeV}^2$ and are reported in Table VI. The four determinations of $Z_P(\mu_{\text{ref}}^2)$ (M1a, M2a, M1b, and M2b) are equally good estimates of the renormalization constant that only differ by $\mathcal{O}(a^2)$ cutoff effects. This implies that using whichever of them leads to equivalent results for the renormalized quark masses and renormalized matrix elements of the pseudoscalar density in the continuum limit. As a check of the good accuracy to which this property

is expected to be satisfied, we show in Fig. 8 the scaling behavior of the difference $\Delta Z_P = Z_P[\text{M2b}] - Z_P[\text{M1a}]$ (in the RI'-MOM scheme at 19 GeV^2), for which all logarithmic divergences cancel and the continuum limit vanishes. A similar behavior, but with smaller $\mathcal{O}(a^2)$ artifacts, is observed for all the analogous differences of the four Z_P determinations in Table VI. Finally, in Table VII, we show the values of $Z_P(19 \text{ GeV}^2)$ converted to the $\overline{\text{MS}}$ scheme.

Since quark masses are generally given in the $\overline{\text{MS}}$ scheme at 2 or 3 GeV , we obtain the corresponding renormalization constants at these scales by using the following evolution factors:

$$Z_P^{\overline{\text{MS}}}(4 \text{ GeV}^2) = 0.83416(86) Z_P^{\overline{\text{MS}}}(19 \text{ GeV}^2), \quad (23)$$

$$Z_P^{\overline{\text{MS}}}(9 \text{ GeV}^2) = 0.92570(34) Z_P^{\overline{\text{MS}}}(19 \text{ GeV}^2), \quad (24)$$

$$Z_P^{\overline{\text{MS}}}(16 \text{ GeV}^2) = 0.98359(19) Z_P^{\overline{\text{MS}}}(19 \text{ GeV}^2). \quad (25)$$

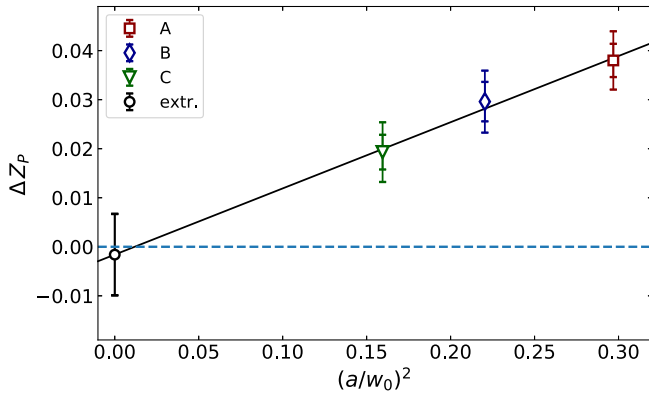


FIG. 8. $\Delta Z_P = Z_P[\text{M2b}] - Z_P[\text{M1a}]$ vs $(a/w_0)^2$ and its (linear) continuum extrapolation. At each finite value of a , the smaller error bars correspond to the first (statistical) error in Table VI, while the larger ones also include the second error in the same Table, which is due to the N^3LO evolution to 19 GeV^2 and is independent from the lattice spacing. Therefore, the continuum limit value and its uncertainty are obtained by taking into account only the statistical errors at finite a .

Our evolution function is accurate at N^3LO [26], i.e., $\mathcal{O}(\alpha_s^3)$, and therefore we estimate the uncertainty due to higher orders as the last known term raised to the power 4/3 (see the second error in the results of Table VI). When computing conversion factors, which are ratios of evolution functions, we add in quadrature the error coming from the numerator and the denominator. We verified that this procedure provides a good estimate of the uncertainty due to higher orders when applied to the N^2LO conversion factors in order to estimate the (known) N^3LO results.

TABLE VII. Results for Z_P at the scale $\mu_{\text{ref}}^2 = 19 \text{ GeV}^2$ converted from RI'-MOM (results of Table VI) to the $\overline{\text{MS}}$ scheme.

$\overline{\text{MS}}, \mu_{\text{ref}}^2 = 19 \text{ GeV}^2$				
β	M1a	M2a	M1b	M2b
1.726	0.569(3)(5)	0.605(3)(5)	0.569(3)(5)	0.614(3)(5)
1.778	0.574(4)(5)	0.601(3)(5)	0.572(3)(5)	0.608(3)(5)
1.836	0.584(3)(5)	0.602(3)(5)	0.584(3)(5)	0.607(3)(5)

TABLE VIII. Values of the bare valence quark mass parameters and the corresponding values of m_π and f_π for each of the ensembles used in the analysis in the pion sector. In the last column the number of gauge configurations analyzed for each ensemble is presented.

Ensemble	$a\mu_\ell$	$a\mu_\ell$	am_π	af_π	Confs
cA211.53.24	0.0053	0.0053	0.16626(51)	0.07106(36)	628
cA211.40.24	0.0040	0.0040	0.14477(70)	0.06809(30)	662
cA211.30.32	0.0030	0.0030	0.12530(16)	0.06674(15)	1237
cA211.12.48	0.0012	0.0012	0.08022(18)	0.06133(33)	322
cB211.25.32	0.0025	0.0025	0.10475(45)	0.05652(38)	400
cB211.25.48	0.0025	0.0025	0.10465(14)	0.05726(12)	314
cB211.14.64	0.0014	0.0014	0.07848(10)	0.05477(12)	437
cB211.072.64	0.00072	0.00072	0.05659(8)	0.05267(14)	374
cC211.20.48	0.0020	0.0020	0.08540(17)	0.04892(13)	890
cC211.06.80	0.0006	0.0006	0.04720(7)	0.04504(10)	401

V. MESON SECTOR ANALYSIS

In this section, we describe the determination of the quark masses taking as input the isosymmetric values of the pion, kaon, and $D_{(s)}$ -meson masses.

A. Methodology

For each ensemble, we compute the two-point function

$$C(t) = \frac{1}{L^3} \sum_{\vec{x}, \vec{z}} \langle 0 | J_{ff'}(\vec{x}, t) J_{ff'}^\dagger(\vec{z}, 0) | 0 \rangle, \quad (26)$$

where $J_{ff'}(x) = \bar{q}_f(x) i\gamma_5 q_{f'}(x)$ is the meson interpolating field with q_f being the valence quark field of flavor $f \in \{\ell, s, c\}$. By ℓ , we denote the average up/down (light) quark. The correlators for the pion and kaon are the same as those used in Ref. [11]. For all mesons, the two valence quarks q_f and $q_{f'}$ are always taken with opposite Wilson parameters, i.e., $r_f = -r_{f'} = 1$, as this choice is known to suppress $O(a^2)$ lattice artifacts [4,7]. For the valence mass parameters, we evaluate correlators at μ_ℓ values equal to its sea counterpart, as well as at three values of the quark mass parameter μ_s in the range of the strange quark masses and four values of the quark mass parameter μ_c in the range of the charm quark masses. The chosen values of valence quark masses are collected in Table VIII and allow for a precise interpolation to the physical strange and charm quark masses as determined by the kaon and D -meson masses in the isosymmetric QCD. The latter ones, following the FLAG report [17], are given by

$$m_K^{\text{isoQCD}} = 494.2(3) \text{ MeV}, \quad (27)$$

$$m_D^{\text{isoQCD}} = 1867.0(4) \text{ MeV}, \quad (28)$$

$$m_{D_s}^{\text{isoQCD}} = 1969.0(4) \text{ MeV}. \quad (29)$$

From the correlator given in Eq. (26), the overlap $\mathcal{S} = |\langle \text{PS} | J_{ff'} | 0 \rangle|^2$ can be extracted using an exponential fit at large time distances

$$C_{\text{PS}}(t) \xrightarrow[t \gg a, (T-t) \gg a]{} \frac{\mathcal{S}}{2m_{\text{PS}}} [e^{-m_{\text{PS}}t} + e^{-m_{\text{PS}}(T-t)}], \quad (30)$$

where m_{PS} is the ground-state mass of a pseudoscalar (PS) meson made of the two valence quarks with flavor f and f' . For maximally twisted quarks, the value of the matrix element \mathcal{S} determines the PS-meson decay constant with no need of any renormalization constant [1], from the formula

$$af_{\text{PS}} = a(\mu_f + \mu_{f'}) \frac{\sqrt{a^4 \mathcal{S}}}{am_{\text{PS}} \sinh(am_{\text{PS}})}. \quad (31)$$

The slight deviation from maximal twist of the ensemble cA211.12.48 is corrected according to Appendix C of Ref. [11].

The global energy scale is set using the isosymmetric QCD inputs (4), and data at different lattice spacings are connected by exploiting the gradient-flow (GF) quantities w_0 [28], $\sqrt{t_0}$ [29], and t_0/w_0 measured in lattice units. Their values have been already determined quite precisely in Ref. [11], namely,⁴

$$w_0 = 0.17383(63) \text{ fm}, \quad (32)$$

$$\sqrt{t_0} = 0.14436(61) \text{ fm}, \quad (33)$$

$$t_0/w_0 = 0.11969(62) \text{ fm}. \quad (34)$$

Nevertheless, in order to take properly into account all the correlations with the meson data, the GF scales are determined again in the present analysis (see the next subsection), obtaining results very compatible with Eqs. (32)–(34).

⁴The result (32) improves drastically our preliminary value of w_0 obtained in Ref. [30]. The improvement is mainly related to a better description of discretization effects on the decay constant f_π [see Eq. (36)] and to the replacement of f_π with the quantity $(f_\pi m_\pi^4)^{1/5}$, which has been found to be less affected by lattice artifacts [11].

B. Light quark mass

The lattice QCD data on the pion mass and decay constant are computed in a unitary setup, i.e., with $\mu_{\text{sea}} = \mu_{\text{valence}} = \mu_\ell$; the values used in this section are reported in Table VIII.

The lattice QCD data on the pion mass and decay constant are analyzed relying on SU(2) chiral perturbation theory (ChPT) using the formulas

$$(m_\pi w_0)^2 = 2(Bw_0)(m_\ell w_0) \times [1 + \xi_\ell \log \xi_\ell + P_1 \xi_\ell + P_2 a^2/w_0^2] K_{M^2}^{\text{FSE}}, \quad (35)$$

$$(f_\pi w_0) = (f w_0) [1 - 2\xi_\ell \log \xi_\ell + P_3 \xi_\ell + P_4 a^2/w_0^2 + a^2 m_\ell P_5] K_f^{\text{FSE}}, \quad (36)$$

where the variable $\xi_\ell = 2Bm_\ell/(16\pi^2 f^2)$ is related to the quark renormalized mass $m_\ell = \mu_\ell/Z_P$. The parameters P_1 and P_3 are related to the low-energy constants $\bar{\ell}_3$ and $\bar{\ell}_4$ by

$$P_1 = -\bar{\ell}_3 - 2 \log(m_\pi^{\text{isoQCD}}/(4\pi f)),$$

$$P_3 = 2\bar{\ell}_4 + 4 \log(m_\pi^{\text{isoQCD}}/(4\pi f)). \quad (37)$$

The quantities $K_{M^2}^{\text{FSE}}$ and K_f^{FSE} represent the finite size effects (FSEs) on the squared pion mass and the pion decay constant, respectively. In Ref. [11], it was shown that SU(2) ChPT at next-to-leading order (NLO) [31] adequately describes our lattice data, once discretization effects proportional both to a^2 and to $a^2 m_\ell$ are included in f_π [see Eq. (36)], while in m_π , the leading lattice artifact is already directly proportional to $a^2 m_\ell$ [see Eq. (35)]. The fit parameters are Bw_0 , $\bar{\ell}_3$, P_2 , $f w_0$, $\bar{\ell}_4$, P_4 , and P_5 . We repeat the fit procedure adopting the values of the renormalization constant Z_P determined using the methods M1a, M1b, M2a, and M2b given in Table VII.

To estimate possible systematics due to the scale setting and the chiral extrapolation, we repeat the analysis using:

- (i) the ratio t_0/w_0 to set the scale;
- (ii) the GF scale $\sqrt{t_0}$ to set the scale;
- (iii) only a combination of two lattice spacing,⁵ namely, $\beta = 1.726$ and $\beta = 1.778$, $\beta = 1.726$ and $\beta = 1.836$, $\beta = 1.778$ and $\beta = 1.836$;
- (iv) only ensembles with pion mass less than 190 MeV and excluding the term P_5 in Eq. (36) from the fit.

The results for the light quark mass m_{ud} are reported in Table IX, where we also include the values of the leading low-energy constants B , f , and $\Sigma^{1/3} = (Bf^2/2)^{1/3}$ as well as the values of $\chi^2/\text{d.o.f.}$ The chiral and continuum extrapolations are illustrated in Fig. 9.

We need now to average the results coming from the different analyses collected in Table IX. To this end,

TABLE IX. The values of the light quark mass, m_{ud} , B , f , and Σ in the $\overline{\text{MS}}$ scheme at 2 GeV obtained using the different determinations of Z_P , labeled M1a, M1b, M2a, and M2b. Results using the GF scale w_0 and all the ensembles of Table VIII are given in the top most panel, using t_0/w_0 in the second panel, using $\sqrt{t_0}$ in the third panel, using w_0 and limiting $m_\pi < 190$ MeV in the fourth panel, using w_0 and only the two coarser lattice spacings in the fifth panel, using w_0 and only the coarser and finest lattice spacings in the sixth panel, and using w_0 and only the two finest lattice spacings in the last panel.

Z_P	m_{ud} (MeV)	B (MeV)	f (MeV)	$\Sigma^{1/3}$	$\chi^2/\text{d.o.f.}$
M1a	3.677(65)	2523(42)	124.02(48)	268.7(1.4)	1.97
M2a	3.694(64)	2512(40)	124.04(50)	268.3(1.4)	1.56
M1b	3.677(66)	2522(43)	124.05(48)	268.7(1.5)	2.53
M2b	3.694(65)	2512(41)	124.02(51)	268.3(1.4)	1.15
t_0/w_0					
M1a	3.722(74)	2493(47)	124.40(49)	268.2(1.6)	2.91
M2a	3.766(73)	2465(45)	124.48(52)	267.3(1.5)	2.54
M1b	3.724(75)	2492(48)	124.42(49)	268.2(1.6)	3.72
M2b	3.771(74)	2462(45)	124.48(52)	267.2(1.6)	1.95
$\sqrt{t_0}$					
M1a	3.696(69)	2510(45)	124.19(48)	268.5(1.5)	2.48
M2a	3.726(68)	2491(43)	124.24(51)	267.9(1.5)	2.06
M1b	3.697(70)	2509(45)	124.22(48)	268.5(1.5)	3.18
M2b	3.729(69)	2490(43)	124.23(51)	267.8(1.5)	1.55
$w_0, m_\pi < 190$ MeV, $P_5 = 0$					
M1a	3.629(81)	2572(55)	122.71(45)	268.5(2.3)	4.72
M2a	3.656(81)	2554(53)	122.56(48)	267.7(2.2)	3.4
M1b	3.623(82)	2577(56)	122.72(45)	268.7(2.3)	6.32
M2b	3.663(82)	2547(54)	122.51(49)	267.4(2.3)	2.2
$w_0, \beta = 1.726$ and $\beta = 1.778$					
M1a	3.83(15)	2420(93)	124.54(83)	265.8(3.2)	0.0953
M2a	3.83(14)	2425(84)	124.57(88)	266.0(2.7)	0.0892
M1b	3.86(14)	2402(86)	124.54(84)	265.1(2.8)	0.0936
M2b	3.80(13)	2446(81)	124.57(88)	266.7(2.6)	0.0895
$w_0, \beta = 1.726$ and $\beta = 1.836$					
M1a	3.660(69)	2539(44)	122.30(49)	266.8(1.5)	0.104
M2a	3.682(67)	2525(43)	122.22(51)	266.2(1.5)	0.0861
M1b	3.657(70)	2541(46)	122.30(49)	266.9(1.6)	0.105
M2b	3.685(68)	2523(43)	122.21(52)	266.1(1.5)	0.0851
$w_0, \beta = 1.778$ and $\beta = 1.836$, $P_5 = 0$					
M1a	3.55(11)	2614(77)	122.64(16)	269.9(2.8)	0.356
M2a	3.587(97)	2588(68)	122.49(17)	268.8(2.5)	0.323
M1b	3.53(10)	2631(73)	122.66(16)	270.5(2.6)	0.362
M2b	3.612(98)	2571(67)	122.44(17)	268.1(2.5)	0.315

we adopt a simple generalization of Eq. (28) of Ref. [12]. For a given observable x , we assume that its probability distribution $f(x)$ is given by

$$f(x) = \sum_{i=1}^N w_i f_i(x), \quad (38)$$

⁵When considering the two finest lattice spacings $\beta = 1.778$ and $\beta = 1.836$, we exclude the term P_5 from the fit of Eq. (36) because all the ensembles have $m_\pi < 260$ MeV.

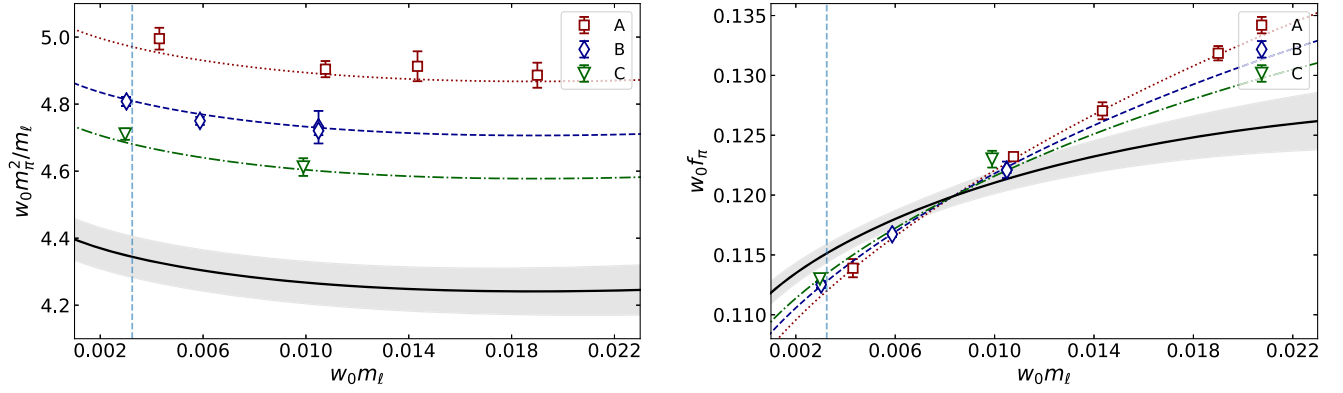


FIG. 9. Chiral and continuum extrapolation of $w_0 m_\pi^2/m_\ell$ (left) and $w_0 f_\pi$ (right) as function of $w_0 m_\ell$ using Eqs. (35) and (36) and Z_P for the M2b method. Different colored bands correspond to different lattice spacings (red for the A ensembles, blue for the B, and green for the C). The gray band is the extrapolation to the continuum limit. Note that for $w_0 f_\pi$ discretization effects proportional both to a^2 and to $a^2 m_\ell$ are visible (see the text).

where w_i are weights to be specified and $f_i(x)$ are the probability distributions corresponding to the individual analyses (labeled with $i = 1, 2, \dots, N$). It is not necessary to specify the form of the individual distributions. It suffices to know that \bar{x}_i and σ_i are the mean value and standard deviation of the distribution $f_i(x)$.

Thus, using Eq. (38), we can represent the combination of the N results of the various analyses in the form

$$\bar{x} \pm \sigma_{\text{stat}} \pm \sigma_{\text{syst}}, \quad (39)$$

where

$$\bar{x} = \sum_{i=1}^N w_i \bar{x}_i, \quad (40)$$

$$\sigma_{\text{stat}}^2 = \sum_{i=1}^N w_i \sigma_i^2, \quad (41)$$

$$\sigma_{\text{syst}}^2 = \sum_{i=1}^N w_i (\bar{x}_i - \bar{x})^2. \quad (42)$$

Equation (41) represents the square of a “statistical” error given by the weighted average of the individual variances, while Eq. (42) corresponds to the square of a “systematic” error related to the spread among the results of the different analyses. The total error σ is given by the sum in quadrature of σ_{stat} and σ_{syst} .

Given the limited number of data points, we refrain in using the values of χ^2 , shown in Table IX, as a quantitative estimate of the quality of the various fits. Instead, since the results of Table IX suggest the dominance of the statistical uncertainties over the systematic ones, a reasonable choice for the weights w_i is $w_i \propto 1/\sigma_i^2$, namely,

$$w_i = \frac{1}{\sigma_i^2} \cdot \frac{1}{\sum_{j=1}^N 1/\sigma_j^2}. \quad (43)$$

Thus, to obtain the value of m_{ud} , we combine the values of Table IX using Eq. (40) for the mean and Eqs. (41)–(42) for the error excluding the analyses with $\chi^2/\text{d.o.f.} > 2.5$ (which leads to a total of 21 analyses). We get in this way

$$m_{ud} = 3.689(80)_{\text{stat}}(63)_{\text{syst}} \text{ MeV} = 3.689(102) \text{ MeV}, \quad (44)$$

TABLE X. Values of the bare valence quark mass parameters and the corresponding values of am_K for each of the ensembles used in the analysis in the kaon. The number of configuration analysed for each ensemble is the reported in Table VIII.

Ensemble	$a\mu_\ell$		$a\mu_s$		am_K		
cA211.53.24	0.00530	0.0176	0.022	0.0264	0.24134(47)	0.26316(47)	0.28340(47)
cA211.40.24	0.00400	0.0176	0.022	0.0264	0.23419(51)	0.25650(52)	0.27709(52)
cA211.30.32	0.00300	0.0176	0.022	0.0264	0.22810(21)	0.25089(22)	0.27185(22)
cA211.12.48	0.00120	0.0176	0.022	0.0264	0.21789(26)	0.24153(29)	0.26319(34)
cB211.25.32	0.00250	0.0148	0.0185	0.0222	0.19212(45)	0.21143(46)	0.22920(47)
cB211.25.48	0.00250	0.0148	0.0185	0.0222	0.19141(19)	0.21067(20)	0.22838(23)
cB211.14.64	0.00140	0.0148	0.0185	0.0222	0.18484(13)	0.20460(15)	0.22268(17)
cB211.072.64	0.00072	0.0148	0.0185	0.0222	0.18038(14)	0.20044(16)	0.21875(18)
cC211.20.48	0.00200	0.0128	0.0161	0.0193	0.16179(16)	0.17878(17)	0.19390(18)
cC211.06.80	0.00060	0.0128	0.0161	0.0193	0.153321(99)	0.17098(11)	0.18656(13)

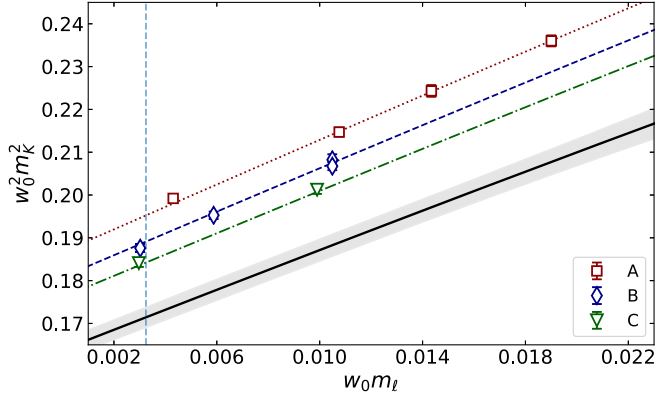


FIG. 10. The red, blue, and green solid lines show the resulting fits using Eq. (49) for ensembles A, B, and C respectively. The gray line shows the continuum extrapolation. We use $(m_s w_0)_{\text{ref}} = 0.080$ and the Z_P computed with method M2b.

$$B = 2516(51)_{\text{stat}}(42)_{\text{syst}} \text{ MeV} = 2516(67) \text{ MeV}, \quad (45)$$

$$f = 122.82(32)_{\text{stat}}(65)_{\text{syst}} \text{ MeV} = 122.82(73) \text{ MeV}, \quad (46)$$

$$\Sigma^{1/3} = 267.6(1.8)_{\text{stat}}(1.1)_{\text{syst}} \text{ MeV} = 267.6(2.1) \text{ MeV}. \quad (47)$$

C. Strange quark mass

In this section, we present our determination of the strange quark mass m_s . For the valence mass parameters, we evaluate correlators for μ_ℓ values equal to its sea counterpart, as well as at three values of the quark mass parameter μ_s in the range of the strange quark masses shown in Table X.

For each ensemble, we perform a linear interpolation of the kaon mass to three reference values of $(m_s w_0)_{\text{ref}} = 0.064, 0.080, 0.095$ using the Ansatz

$$m_K^2 = a + b m_s w_0. \quad (48)$$

A similar interpolation is also performed for the other GF scales t_0/w_0 and $\sqrt{t_0}$. Then, for each value of $(m_s w_0)_{\text{ref}}$, we extrapolate to the continuum limit and to the isosymmetric QCD point using the value of $m_\ell = m_{ud}$ determined in the previous section and our best fit to the data for m_K according to the Ansatz

$$(m_K w_0)^2 = P_0(m_\ell w_0 + m_s w_0) \times [1 + P_1 m_\ell w_0 + P_2 m_\ell^2 w_0^2 + P_3 a^2/w_0^2]. \quad (49)$$

At NLO order of SU(2) ChPT, there are no finite volume effects on the kaon mass, and in Ref. [11], it has been shown that the lattice QCD data on the kaon masses agree with this prediction. The fit parameters in Eqs. (49) are P_0 , P_1 , P_2 , and P_3 , while the LO low-energy constants f and B are taken from our pion sector fit. The quality of the resulting fit to Eq. (49) is shown in Fig. 10 as an example

TABLE XI. The values of the strange quark mass, m_s , in the $\overline{\text{MS}}$ scheme at 2 GeV and the ratio m_s/m_{ud} obtained using the different determinations of Z_P , labeled M1a, M1b, M2a, and M2b. Results using the GF scale w_0 and all the ensembles of Table X are given in the top most panel, using t_0/w_0 in the second panel, using $\sqrt{t_0}$ in the third panel, using w_0 and limiting $m_\pi < 190$ MeV in the fourth panel, using w_0 and only the two coarser lattice spacings in the fifth panel, using w_0 and only the coarser and finest lattice spacings in the sixth panel, and using w_0 and only the two finest lattice spacings in the last panel. To determine the ratio m_s/m_{ud} , we use the values of m_{ud} from Table IX.

Z_P	m_s (MeV)	m_s/m_{ud}	$\chi^2/\text{d.o.f.}$
M1a	100.4(1.6)	27.32(21)	1
M2a	100.9(1.5)	27.32(22)	1
M1b	100.6(1.6)	27.37(22)	1.7
M2b	101.0(1.5)	27.34(22)	0.76
t_0/w_0			
M1a	101.6(1.8)	27.28(23)	1.1
M2a	102.8(1.7)	27.30(24)	1.3
M1b	101.8(1.8)	27.34(23)	1.9
M2b	103.1(1.7)	27.34(24)	1
$\sqrt{t_0}$			
M1a	101.0(1.7)	27.31(22)	1.1
M2a	101.8(1.6)	27.32(23)	1.2
M1b	101.2(1.7)	27.37(22)	1.8
M2b	102.0(1.6)	27.35(23)	0.9
$w_0, m_\pi < 190 \text{ MeV}, P_2 = 0$			
M1a	100.9(1.8)	27.82(40)	3.6
M2a	101.4(1.7)	27.73(37)	4
M1b	101.1(1.8)	27.90(38)	6.1
M2b	101.4(1.7)	27.68(37)	2.9
$w_0, \beta = 1.726 \text{ and } \beta = 1.778 \text{ only}, P_2 = 0$			
M1a	103.4(3.7)	26.96(29)	0.34
M2a	103.1(3.2)	26.94(31)	0.46
M1b	104.1(3.4)	26.95(29)	0.42
M2b	102.3(3.0)	26.94(31)	0.52
$w_0, \beta = 1.726 \text{ and } \beta = 1.836 \text{ only}, P_2 = 0$			
M1a	99.8(1.6)	27.26(22)	0.18
M2a	100.4(1.5)	27.26(22)	0.18
M1b	99.7(1.7)	27.26(22)	0.16
M2b	100.5(1.6)	27.26(22)	0.17
$w_0, \beta = 1.778 \text{ and } \beta = 1.836 \text{ only}, P_2 = 0$			
M1a	97.7(2.8)	27.54(29)	0.21
M2a	98.8(2.4)	27.55(30)	0.32
M1b	97.1(2.6)	27.53(29)	0.28
M2b	99.5(2.5)	27.55(30)	0.37

for the specific determination of Z_P . Other determinations yield similar results.

The last step of the analysis is an interpolation using Eq. (48) to find the value of m_s that reproduces $m_K^{\text{isoQCD}} = 494.2(3) \text{ MeV}$ given in Eq. (27). As in the case of the pion, to estimate the systematic errors related to the scale setting, in the chiral extrapolation and the continuum limit, we repeat the analyses using two different GF scales, excluding the

TABLE XII. Values of the bare valence quark mass parameters and the corresponding values of am_D from the GEVP analysis [32] for each of the ensembles used in the analysis in the D meson. The number of configuration analyzed for each ensemble is the reported in Table VIII.

Ensemble	$a\mu_\ell$	$a\mu_c$				am_D			
cA211.53.24	0.00530	0.2077	0.2336	0.2596	0.2856	0.7694(12)	0.8207(12)	0.8703(13)	0.9179(14)
cA211.40.24	0.00400	0.2077	0.2336	0.2596	0.2856	0.7676(13)	0.8190(15)	0.8686(16)	0.9164(18)
cA211.30.32	0.00300	0.2077	0.2336	0.2596	0.2856	0.76284(67)	0.81428(73)	0.86387(80)	0.91167(86)
cA211.12.48	0.00120	0.2077	0.2336	0.2596	0.2856	0.7567(17)	0.8078(20)	0.8570(23)	0.9044(26)
cB211.25.48	0.00250	0.1745	0.1962	0.2181	0.2399	0.6477(11)	0.6919(12)	0.7349(12)	0.7762(13)
cB211.14.64	0.00140	0.1745	0.1962	0.2181	0.2399	0.64373(70)	0.68816(79)	0.73133(87)	0.77284(96)
cB211.072.64	0.00072	0.1745	0.1962	0.2181	0.2399	0.6415(13)	0.6860(15)	0.7292(16)	0.7709(18)
cC211.20.48	0.00200	0.1526	0.1716	0.1907	0.2098	0.55934(60)	0.59821(64)	0.63589(68)	0.67237(73)
cC211.06.80	0.00060	0.1526	0.1716	0.1907	0.2098	0.5533(11)	0.5921(12)	0.6297(13)	0.6660(15)

ensembles with pion mass larger than 190 MeV and the term proportional to P_2 in Eq. (49), and with only pairs of values of the lattice spacing. The results are shown in Table XI.

We use the same procedure as for m_{ud} to obtain the mean value, statistical, and systematic errors for m_s using Eqs. (40)–(42) excluding the analyses with $\chi^2/\text{d.o.f.} > 2.5$. We find in the $\overline{\text{MS}}$ scheme at 2 GeV

$$m_s = 101.0(1.9)_{\text{stat}}(1.3)_{\text{syst}} \text{ MeV} = 101.0(2.3) \text{ MeV}, \quad (50)$$

$$\frac{m_s}{m_{ud}} = 27.30(24)_{\text{stat}}(14)_{\text{syst}} = 27.30(28). \quad (51)$$

D. Charm quark mass

In this section, we present our determination of the mass of the charm quark obtained by analyzing D - and D_s -meson masses, following a strategy similar to the one presented for the determination of m_s . For the valence mass parameters, we evaluate correlators for μ_ℓ values equal to its sea counterpart, as well as at four values of the quark mass parameter μ_c in the range of the charm mass. In the case of the D_s meson, we also use three values of the quark mass parameter μ_s equal to the values used in the kaon analysis (see Table X). The values for the D -meson masses are given in Table XII, while the ones for the D_s -meson are given in Table XIII. The D - and D_s -meson correlators are computed using both smeared and local interpolating fields. Using the four combinations of smeared-smeared, smeared-local, and local-local correlators, we construct a 2×2 matrix and perform a generalized eigenvalue problem (GEVP) analysis [32] to extract the mass of the D - and D_s -mesons.⁶ We employ Jacobi smearing for the quark

fields [33], combined with array processor experiment (APE) smearing of the gauge links [34] used in the Jacobi smearing function. The values of m_D and m_{D_s} used in this analysis are reported in Tables XII and XIII.

Analogously to the case of the analysis for the strange quark mass determination, we interpolate the D and D_s masses to three reference values given by $(m_c w_0)_{\text{ref}} = 0.94, 1.04, 1.08$ using the Ansatz

$$m_{D_s} = a + b m_c w_0. \quad (52)$$

For the D_s meson, we also perform an interpolation to the mass m_s given in Table XI. At each of the reference charm quark masses, we extrapolate to the continuum and to the isospin-symmetric QCD (isoQCD) light quark mass $m_\ell = m_{ud}$ using the following polynomials in m_ℓ ,

$$m_D = P_0 + P_1 m_\ell w_0 + P_2 a^2 / w_0^2, \quad (53)$$

$$m_{D_s} = P_0^s + P_1^s m_\ell w_0 + P_2^s a^2 / w_0^2, \quad (54)$$

where P_j and P_j^s , $j = 0, 1, 2$, are fit parameters. For each reference mass $(m_c w_0)_{\text{ref}}$, we compute the masses m_D and m_{D_s} in the continuum limit at the isoQCD value of $m_\ell = m_{ud}$ given in Table IX. We then perform an interpolation in m_c with the Ansatz given in Eq. (52) to compute the value of m_c that reproduces the isoQCD masses of the D or D_s mesons, given in Eqs. (28) and (29). We note that the analysis is done separately using either the D or the D_s meson.

The resulting fits to Eqs. (53) and (54) for the D and D_s mesons are shown in Fig. 11 for the case where Z_P is determined from the M2b method.

The values in physical units that we obtain for the m_c mass are shown in Table XIV.

We combine all the values given in Table XIV excluding the analyses with $\chi^2/\text{d.o.f.} > 2.5$ as in the case of the pion and kaon with Eqs. (40)–(42). We find

⁶As discussed in Ref. [32], the mass of the ground state is estimated through an average over the values in the plateau region using the principal correlator corresponding to the smallest eigenvalue $\lambda_0(t, t_0)$ obtained from the GEVP for a suitable choice of the reference time t_0 . In other words, we fit $\lambda_0(t, t_0) = C(e^{-m_{D,D_s}(t-t_0)} + e^{-m_{D,D_s}((T-t)-t_0)})$.

TABLE XIII. Values of the bare valence quark mass parameters and the corresponding values of am_{D_s} from the GEVP analysis [32] for each of the ensembles used in the analysis in the D_s meson. The strange quark masses m_s are the same used in the kaon sector Table X. The number of configurations analyzed for each ensemble is the reported in Table VIII.

Ensemble	$a\mu_\ell$	$a\mu_c$				am_{D_s}			
cA211.53.24	0.0176	0.2077	0.2336	0.2596	0.2856	0.79724(78)	0.84790(81)	0.89693(85)	0.94414(88)
	0.0220	0.2077	0.2336	0.2596	0.2856	0.80696(72)	0.85738(75)	0.90619(78)	0.95323(81)
	0.0264	0.2077	0.2336	0.2596	0.2856	0.81656(67)	0.86673(69)	0.91534(72)	0.96220(75)
cA211.40.24	0.0176	0.2077	0.2336	0.2596	0.2856	0.79838(58)	0.84918(63)	0.89825(69)	0.94561(75)
	0.0220	0.2077	0.2336	0.2596	0.2856	0.80789(50)	0.85844(54)	0.90729(59)	0.95447(64)
	0.0264	0.2077	0.2336	0.2596	0.2856	0.81733(44)	0.86763(48)	0.91626(52)	0.96326(56)
cA211.30.32	0.0176	0.2077	0.2336	0.2596	0.2856	0.79610(28)	0.84675(30)	0.89567(32)	0.94289(34)
	0.0220	0.2077	0.2336	0.2596	0.2856	0.80573(26)	0.85613(27)	0.90484(28)	0.95189(30)
	0.0264	0.2077	0.2336	0.2596	0.2856	0.81527(24)	0.86544(25)	0.91395(26)	0.96082(27)
cA211.12.48	0.0176	0.2077	0.2336	0.2596	0.2856	0.79416(39)	0.84469(42)	0.89347(45)	0.94055(48)
	0.0220	0.2077	0.2336	0.2596	0.2856	0.80385(35)	0.85417(37)	0.90278(39)	0.94973(42)
	0.0264	0.2077	0.2336	0.2596	0.2856	0.81345(32)	0.86355(33)	0.91199(35)	0.95878(37)
cB211.25.48	0.0148	0.1745	0.1962	0.2181	0.2399	0.67488(25)	0.71849(26)	0.76093(27)	0.80181(29)
	0.0185	0.1745	0.1962	0.2181	0.2399	0.68310(20)	0.72652(21)	0.76881(22)	0.80956(23)
	0.0222	0.1745	0.1962	0.2181	0.2399	0.69127(17)	0.73451(17)	0.77664(18)	0.81726(19)
cB211.14.64	0.0148	0.1745	0.1962	0.2181	0.2399	0.67415(20)	0.71771(21)	0.76010(22)	0.80094(24)
	0.0185	0.1745	0.1962	0.2181	0.2399	0.68243(18)	0.72579(19)	0.76803(20)	0.80873(21)
	0.0222	0.1745	0.1962	0.2181	0.2399	0.69064(16)	0.73381(17)	0.77589(18)	0.81646(18)
cB211.072.64	0.0148	0.1745	0.1962	0.2181	0.2399	0.67351(22)	0.71707(24)	0.75948(27)	0.80035(31)
	0.0185	0.1745	0.1962	0.2181	0.2399	0.68188(19)	0.72526(21)	0.76752(23)	0.80826(26)
	0.0222	0.1745	0.1962	0.2181	0.2399	0.69016(17)	0.73336(18)	0.77547(21)	0.81608(23)
cC211.20.48	0.0128	0.1526	0.1716	0.1907	0.2098	0.58322(25)	0.62162(26)	0.65893(27)	0.69511(28)
	0.0161	0.1526	0.1716	0.1907	0.2098	0.59050(22)	0.62874(23)	0.66592(24)	0.70199(25)
	0.0193	0.1526	0.1716	0.1907	0.2098	0.59752(20)	0.63561(21)	0.67266(21)	0.70863(22)
cC211.06.80	0.0128	0.1526	0.1716	0.1907	0.2098	0.58181(21)	0.62019(23)	0.65748(25)	0.69365(28)
	0.0161	0.1526	0.1716	0.1907	0.2098	0.58919(19)	0.62741(20)	0.66457(22)	0.70063(24)
	0.0193	0.1526	0.1716	0.1907	0.2098	0.59629(17)	0.63436(18)	0.67139(20)	0.70734(21)

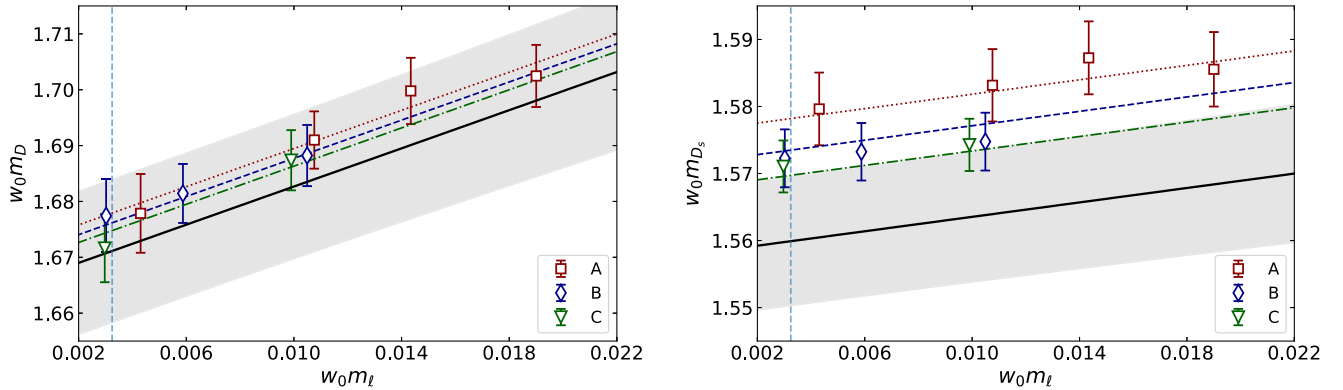


FIG. 11. Results obtained by fitting to Eq. (53) for the D meson (left panel) and Eq. (54) for the D_s meson (right panel) using the value of Z_P extracted from the M2b method and using w_0 to set the scale. The notation is the same as that of Fig. 10.

TABLE XIV. Values of the charm quark mass m_c in the $\overline{\text{MS}}$ scheme at 3 GeV and the ratio m_c/m_s from the analysis of the D and D_s meson, for different determinations of Z_P and GF scales. Results using the GF scale w_0 and all the ensembles of Table XII are given in the top most panel, using t_0/w_0 in the second panel, using $\sqrt{t_0}$ in the third panel, using w_0 and limiting $m_\pi < 190$ MeV in the fourth panel, using w_0 and only the two coarser lattice spacings in the fifth panel, using w_0 and only the coarser and finest lattice spacings in the sixth panel, and using w_0 and only the two finest lattice spacings in the last panel. To determine the ratio m_c/m_s we use the values of m_s from Table XI.

Z_P	D			D_s		
	m_c (MeV)	m_c/m_s	$\chi^2/\text{d.o.f.}$	m_c (MeV)	m_c/m_s	$\chi^2/\text{d.o.f.}$
M1a	1041(14)	11.504(76)	0.25	1039(13)	11.476(70)	0.62
M2a	1041(13)	11.443(76)	0.16	1038(12)	11.414(69)	0.45
M1b	1043(14)	11.496(77)	0.45	1040(13)	11.463(71)	1.2
M2b	1039(13)	11.418(78)	0.14	1037(12)	11.397(71)	0.21
t_0/w_0						
M1a	1042(15)	11.385(84)	0.12	1038(13)	11.342(79)	0.36
M2a	1045(14)	11.283(85)	0.15	1041(12)	11.235(78)	0.25
M1b	1043(15)	11.375(86)	0.2	1039(14)	11.322(81)	0.76
M2b	1045(14)	11.248(86)	0.25	1041(13)	11.206(80)	0.1
$\sqrt{t_0}$						
M1a	1041(14)	11.448(79)	0.16	1038(13)	11.412(74)	0.48
M2a	1043(13)	11.368(80)	0.13	1039(12)	11.329(73)	0.35
M1b	1043(14)	11.439(81)	0.29	1039(14)	11.396(75)	0.96
M2b	1042(13)	11.338(81)	0.18	1039(12)	11.306(75)	0.15
$w_0, m_\pi < 190$ MeV, $P_2 = 0$						
M1a	1042(16)	11.46(14)	0.099	1037(13)	11.396(96)	1.3
M2a	1041(15)	11.39(14)	0.028	1035(12)	11.333(97)	0.8
M1b	1043(16)	11.45(14)	0.38	1037(14)	11.380(96)	2.6
M2b	1039(15)	11.37(14)	0.25	1034(12)	11.316(98)	0.26
$w_0, \beta = 1.726$ and $\beta = 1.778$ only, $P_2 = 0$						
M1a	1057(31)	11.34(16)	0.12	1062(29)	11.41(15)	0.043
M2a	1046(26)	11.26(16)	0.13	1052(24)	11.32(15)	0.045
M1b	1063(28)	11.34(16)	0.11	1069(26)	11.40(15)	0.04
M2b	1037(24)	11.25(16)	0.13	1042(22)	11.31(15)	0.046
$w_0, \beta = 1.726$ and $\beta = 1.836$ only, $P_2 = 0$						
M1a	1038(14)	11.545(76)	0.23	1036(13)	11.522(66)	0.097
M2a	1039(13)	11.487(77)	0.24	1036(12)	11.456(67)	0.096
M1b	1037(14)	11.546(76)	0.21	1035(14)	11.523(66)	0.086
M2b	1039(13)	11.474(77)	0.23	1036(12)	11.441(68)	0.095
$w_0, \beta = 1.778$ and $\beta = 1.836$ only, $P_2 = 0$						
M1a	1029(28)	11.68(12)	0.082	1019(25)	11.576(87)	0.0033
M2a	1037(24)	11.65(12)	0.12	1027(22)	11.534(88)	0.0045
M1b	1022(26)	11.68(12)	0.097	1014(23)	11.585(86)	0.0045
M2b	1044(24)	11.64(12)	0.13	1033(21)	11.520(89)	0.005

$$m_c = 1039(15)_{\text{stat}}(6)_{\text{syst}} \text{ MeV} = 1039(16) \text{ MeV}, \quad (55)$$

$$\frac{m_c}{m_s} = 11.43(9)_{\text{stat}}(10)_{\text{syst}} = 11.43(13), \quad (56)$$

where the charm quark mass is given in the $\overline{\text{MS}}$ at 3 GeV.

VI. BARYON SECTOR ANALYSIS

In the baryon sector, we use the nucleon and pion masses to set the scale and determine the light quark mass. We use

the $\Omega^-(sss)$ and the $\Lambda_c(udc)$ masses to determine, respectively, the strange and charm quark masses. The range of validity of ChPT in the baryon sector is more limited as compared to that in the pion sector, and thus we restrict ourselves to using pion masses up to 260 MeV.

A. Methodology

In order to compute the baryon masses, we construct the following two-point correlation functions at zero momentum, defined as

$$C_B^\pm(t) = \sum_{\vec{x}} \langle 0 | \frac{1}{4} \text{Tr}[(1 \pm \gamma_0) J_{B(qq'q'')}(\vec{x}, t) \bar{J}_{B(qq'q'')}(\vec{0}, 0)] | 0 \rangle, \quad (57)$$

where $J_{B(qq'q'')}$ is the interpolating operator for the baryon $B(q, q', q'')$ with $q, q',$ and $q'' \in \{l, s, c\}$. In this work, we increase statistics by considering both $\frac{1}{2}(1 \pm \gamma_0)$ projectors. For the interpolating fields of the nucleon, the Ω , and the Λ_c we take, respectively,

$$\begin{aligned} J_N &= \epsilon^{abc} (u_a^T C \gamma_5 d_b) u_c, \\ J_\Omega &= \epsilon^{abc} (s_a C \gamma_\mu s_b) s_c, \\ J_{\Lambda_c} &= \frac{1}{\sqrt{6}} \epsilon^{abc} [2(u_a^T C \gamma_5 d_b) c_c + (u_a^T C \gamma_5 c_a) d_c \\ &\quad - (d_a^T C \gamma_5 c_b) u_c], \end{aligned} \quad (58)$$

where latin indices refer to color, ϵ^{abc} is the antisymmetric tensor, and C is the charge conjugation matrix.

In order to suppress contributions from excited states, we apply Gaussian smearing to each quark field $q(\vec{x}, t)$. The smeared quark field is given by $q_{\text{smeared}}(\vec{x}, t) = \sum_{\vec{y}} F(\vec{x}, \vec{y}; U(t)) q(\vec{y}, t)$, where F is the gauge-invariant smearing function

$$F(\vec{x}, \vec{y}; U(t)) = (1 + \alpha H)^n(\vec{x}, \vec{y}; U(t)), \quad (59)$$

constructed from the hopping matrix understood as a matrix in coordinate, color, and spin space,

$$H(\vec{x}, \vec{y}, U(t)) = \sum_{i=1}^3 (U_i(\vec{x}, t) \delta_{\vec{x}, \vec{y} - a\hat{i}} + U^\dagger(\vec{x} - a\hat{i}, t) \delta_{\vec{x}, \vec{y} + a\hat{i}}). \quad (60)$$

In addition, we apply APE smearing to the spatial links that enter the hopping matrix H . Different Gaussian smearing is applied to the light and strange quarks. The parameters of the Gaussian and APE smearing for each ensemble for the light and strange quarks are given in Table XV. The charm quark interpolating fields are not smeared.

Two-point correlators for the Ω and Λ_c are computed for each ensemble at three different values of the valence strange and charm quark masses $a\mu_s$ and $a\mu_c$. For each value, an analysis of the two-point correlator is carried out in order to determine the masses m_Ω and m_{Λ_c} as a function of μ_s and μ_c , respectively. The effective mass

$$am_B^{\text{eff}} = \log \left(\frac{C_B(t)}{C_B(t+a)} \right) \quad (61)$$

can be written using the spectral decomposition of the two-point correlators as

TABLE XV. Parameters n and α entering the Gaussian smearing in Eq. (59) per ensemble for the light and strange quark interpolating fields. The parameters for the APE smearing are kept the same for all ensembles. They are $n_{\text{APE}} = 50$ and $\alpha_{\text{APE}} = 0.5$.

Ensemble	Light		Strange	
	n	α	n	α
cA211.30.32	40	1.0	25	4.0
cA211.12.48	50	1.0	25	4.0
cB211.25.32	40	1.0	25	4.0
cB211.25.48	40	1.0	25	4.0
cB211.14.64	70	1.0	25	4.0
cB211.072.64	125	0.4	25	4.0
cC211.20.48	40	1.0	25	1.0
cC211.06.80	140	1.0	25	1.0

$$am_B^{\text{eff}} \approx am_B + \log \left(\frac{1 + \sum_{j=1}^K c_j e^{-\Delta_j t}}{1 + \sum_{j=1}^K c_j e^{-\Delta_j(t+a)}} \right), \quad (62)$$

where Δ_j is the mass difference of the j th excited state with respect to the ground state mass m_B . We consider one-, two-, and three-state fits by taking $K = 0, 1, 2$ in Eq. (62). This allows us to check the consistency in our determination of the ground state mass m_B . Since statistical errors are larger for baryons as compared to those of mesons and grow rapidly with increasing time separation t , it is important to identify the ground state for as small a time separation as possible, so that we can be confident that excited are sufficiently suppressed. Our procedure for identifying m_B is as follows:

- (1) We keep the upper time used in the fit constant. The upper time is chosen so that statistical errors are reliably evaluated.
- (2) We fit the effective mass keeping two excited states; i.e., we take $K = 2$ in Eq. (62) and vary the lower time used in the fit t_{low}^{3st}/a from 1 to 3. We choose the parameters of the fit that has the smallest t_{low}^{3st} for which $\chi^2/\text{d.o.f.} \lesssim 1$. This determines m_B^{3st} .
- (3) We then fit the effective mass including one excited state; i.e., we set $K = 1$ in Eq. (62) and vary t_{low}^{2st} for $t_{\text{low}}^{2st} > t_{\text{low}}^{3st}$ until the extracted mass m_B^{2st} satisfies the criterion $|m_B^{2st} - m_B^{3st}| < \delta m_B^{2st}$, where δm_B^{2st} is the statistical error on m_B^{2st} (i.e., the difference in the central values of the baryon masses extracted using one and two excited states are compatible within the statistical error of m_B^{2st}).
- (4) Having determined m_B^{2st} , we make a single state fit; i.e., we set $K = 0$ in Eq. (62) and vary the lower value of t . We choose $t_{\text{low}}^{1st} > t_{\text{low}}^{2st}$ and take the smallest value that satisfies $|m_B^{1st} - m_B^{2st}| < \delta m_B^{1st}$, where δm_B^{1st} is the statistical error on m_B^{1st} , provided $\chi^2/\text{d.o.f.} \sim 1$. We used m_B^{1st} as our final value for m_B .

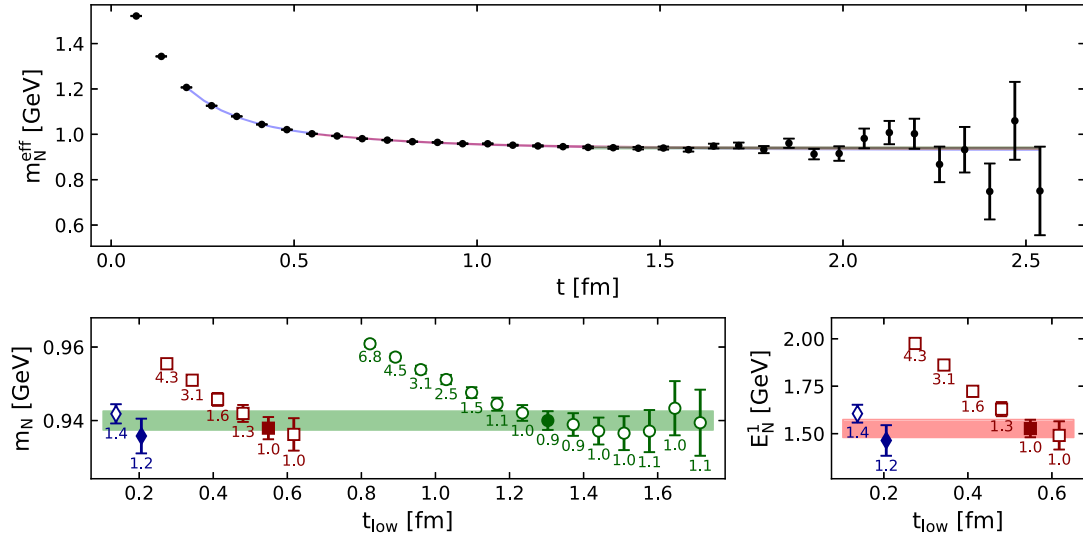


FIG. 12. Upper panel: we show the nucleon effective mass $m_N^{\text{eff}}(t)$ as a function of t for the cC211.06.80 ensemble. Lower left panel: we show the convergence of the extracted value of m_N as a function of the lowest time t_{low} used in the fit when we include one state in the fit (green open circles), when we include two states (open red squares) and when we include three states (open blue rhombus). Lower right panel: the same as the lower left panel but for the values extracted for the mass of the first excited state. The filled symbols and green and red bands show the values we pick for m_N and for the mass of the excited state m_{Roper} , respectively. For each point, we give the $\chi^2/\text{d.o.f.}$ of the fit.

We illustrate our analysis for the extraction of the masses by giving representative examples for the nucleon, Ω^- and Λ_c^- . In all cases, we use correlation functions with smeared sources and for the ensembles listed in Table XVI. In Fig. 12, we show an example of the results obtained using the nucleon correlators for the cC211.06.80 ensemble, and in Table XVI, we give the number of configurations and source positions used, the fit ranges for the one-, two-, and three-state fits, as well as the extracted nucleon mass and the $\chi^2/\text{d.o.f.}$ As can be seen, the mass of the first excited state converges to a value compatible with the mass of the Roper for the physical point ensembles.

The nucleon-pion state, although it has lower energy, it is volume suppressed. In our two-state fits to extract the energy of the first excited state, we find that the coefficient of the second exponential compared to that of the ground state is of order 1. This is to be contrasted with the chiral perturbation theory analysis of Ref. [35], which predicts a few percent for two-particle states. This indicates that the contribution of two particles is suppressed.

We analyze in a similar way the effective mass defined by the Ω correlator given in Eq. (57). In Fig. 13, we show an example of the effective mass m_Ω^{eff} for the cB211.072.64 ensemble at $\mu_s = 0.017, 0.0195$, and 0.022 . As can be seen,

TABLE XVI. We give for each ensemble the resulting values of am_N , when using one-state (fourth main column), two-state (fifth main column), and three-state (sixth main column) fits, $\bar{\chi}^2 \equiv \chi^2/\text{d.o.f.}$ is the reduced χ^2 , n_{conf} is the number of configurations analyzed, n_{srcs} is the number of two-point functions generated per configuration at different source positions, and $[t_{\text{low}}, t_{\text{max}}]$ is the fitting range. We also show the values for the pion mass computed on the same statistics, am_π , noticing that they are compatible with those given in Table I.

Ensemble	am_π	n_{conf}	n_{srcs}	t_{max}/a	One-state fit			Two-state fit			Three-state fit		
					t_{low}/a	$\bar{\chi}^2$	am_N	t_{low}/a	$\bar{\chi}^2$	am_N	t_{low}/a	$\bar{\chi}^2$	am_N
cA211.30.32	0.12525(13)	287	121	25	12	0.9	0.5075(18)	4	0.8	0.5077(16)	2	0.8	0.5068(22)
cA211.12.48	0.080281(75)	325	160	27	15	1.1	0.4566(22)	7	1.4	0.4561(33)	2	1.4	0.4589(23)
cB211.25.32	0.10521(21)	395	121	27	16	0.5	0.4325(38)	7	0.5	0.4288(39)	2	0.8	0.4301(47)
cB211.25.48	0.104408(59)	281	128	33	17	0.7	0.4307(18)	5	1.5	0.43097(94)	2	1.7	0.4305(11)
cB211.14.64	0.078429(38)	194	128	33	18	2.4	0.4015(28)	7	1.7	0.3977(33)	2	1.8	0.3990(42)
cB211.072.64	0.056578(20)	751	264	34	18	1.4	0.3822(17)	7	1.1	0.3813(15)	2	1.3	0.3823(16)
cC211.20.48	0.086098(86)	205	121	33	17	1.2	0.3664(17)	8	1.4	0.3669(20)	2	1.2	0.3658(18)
cC211.06.80	0.047248(19)	401	650	38	19	0.9	0.32679(88)	8	1.0	0.3261(11)	3	1.2	0.3253(16)

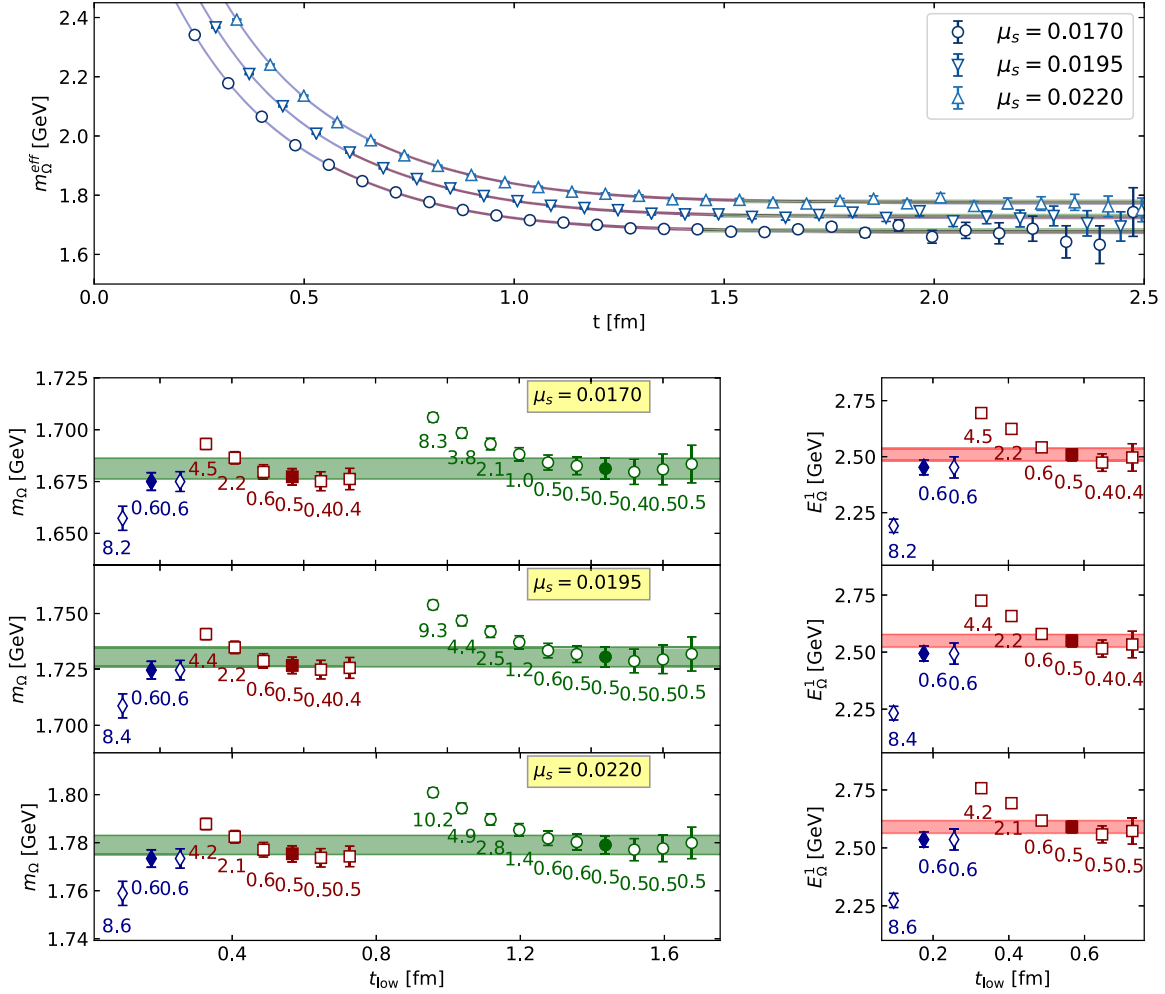


FIG. 13. The same as in Fig. 12 but for the case of Ω^- using the cB211.072.64 ensemble for the three values of μ_s given in the figure legend.

we obtain accurate results that allow us to perform a fit including up to the second excited state. We fix the maximum time for these fits to be $t_{\max}/a = 34$. The convergence of the effective mass for Ω^- as we vary t_{low} is demonstrated when using one-, two-, and three-state fits. In a similar manner, the convergence of the first excited energy E_{Ω}^1 is demonstrated by varying t_{low} . We employ the criterion described above to choose the value of m_{Ω} from the one-state fit at each μ_s . We note that for all the three values of μ_s we find the same t_{low} . The masses extracted are given in Table XVII, where we also quote the reduced- χ^2 , $\bar{\chi}^2 \equiv \chi^2/\text{d.o.f.}$, of the various fits.

The analysis of the two-point correlator for the Λ_c proceeds in an analogous manner. We illustrate the results for the cB211.072.64 ensemble in Fig. 14 for two different values of the charm mass parameter μ_c . From the study of the Ω^- mass, we find that there is strong correlation among the data for the three values of μ_s as demonstrated in Fig. 16, and, thus, for Λ_c , we opt to use two different values

of μ_c in the interpolation. Since Λ_c is heavier and decays faster, a three-state fit is not possible, and we limit ourselves to comparing one- and two-state fits. The masses extracted, the statistics used, and the value of $\bar{\chi}^2$ are given in Table XVIII.

In what follows, we will use the values of m_N , m_{Ω} , and m_{Λ_c} extracted from the one-state fit given in Tables XVI–XVIII, respectively, to determine the light, strange, and charm quark masses. In order to estimate the systematic error due to the fit range, we will also use the values for the masses extracted from the one-state fit at $t_{\text{low}}/a + 1$.

B. Light quark mass

We use the ChPT expression of Eq. (5) to extrapolate to the physical point. To one-loop order in ChPT [up to which the nucleon mass is expanded in Eq. (5)], we can substitute the pion mass by $m_{\pi}^2 = 2Bm_{ud}(1 + c_2 a^2)$ to obtain the expansion

TABLE XVII. We give the mass of Ω^- in lattice units using one- (fourth main column that includes t_{low}/a and the reduced $\bar{\chi}^2$), two- (fifth main column), and three- (sixth main column) state fits to the effective mass. In the second main column, we give the number of configurations n_{conf} , the number of two-point function per configuration n_{srcs} , and t_{max}/a . In the last main column, we give the fit parameters A_Ω in lattice units and B_Ω defined in Eq. (65) using the Ω^- mass from the one-state fit.

Ensemble	n_{conf}	n_{srcs}	t_{max}/a	$a\mu_s$	One-state fit			Two-state fit			Three-state fit			aA_Ω	B_Ω/Z_P
					t_{low}/a	$\bar{\chi}^2$	am_Ω	t_{low}/a	$\bar{\chi}^2$	am_Ω	t_{low}/a	$\bar{\chi}^2$	am_Ω		
cA211.30.32	1260	16	28	0.0182	14	1.0	0.7890(22)	4	1.1	0.7874(19)	2	1.1	0.7859(30)	0.645(4)	7.89(11)
				0.0227	14	1.3	0.8252(18)	4	1.2	0.8237(17)	2	0.8	0.8230(22)		
				0.0273	14	1.2	0.8610(15)	4	1.1	0.8595(15)	2	0.9	0.8590(19)		
cA211.12.48	341	64	29	0.0182	16	0.4	0.7797(27)	4	0.6	0.7796(15)	2	0.5	0.7783(25)	0.634(5)	8.00(13)
				0.0227	16	0.5	0.8164(21)	4	0.6	0.8164(13)	2	0.6	0.8155(21)		
				0.0273	16	0.6	0.8527(17)	4	0.6	0.8527(11)	2	0.6	0.8521(17)		
cB211.25.32	492	16	28	0.0148	16	0.9	0.6684(36)	8	1.2	0.6652(66)	2	1.0	0.6630(86)	0.551(7)	7.94(23)
				0.0185	16	0.9	0.6986(28)	8	1.1	0.6959(46)	2	0.9	0.6942(55)		
				0.0222	16	0.8	0.7274(23)	8	1.0	0.7250(37)	2	0.9	0.7236(42)		
cB211.25.48	651	32	34	0.0148	18	1.6	0.6666(21)	6	1.0	0.6656(17)	2	1.1	0.6649(24)	0.551(4)	7.79(13)
				0.0185	18	1.4	0.6959(16)	6	0.9	0.6947(14)	2	0.9	0.6939(22)		
				0.0222	18	1.2	0.7244(13)	6	0.8	0.7232(13)	2	0.9	0.7224(20)		
cB211.14.64	446	16	32	0.0148	18	0.4	0.6603(35)	6	0.8	0.6583(31)	2	0.7	0.6528(63)	0.542(6)	8.00(21)
				0.0185	18	0.5	0.6905(28)	6	0.8	0.6883(27)	2	0.7	0.6838(53)		
				0.0222	18	0.5	0.7197(23)	6	0.8	0.7174(25)	2	0.7	0.7136(46)		
cB211.072.64	770	32	34	0.0170	18	0.5	0.6799(20)	7	0.5	0.6783(16)	2	0.6	0.6774(17)	0.545(4)	7.90(12)
				0.0195	18	0.5	0.6998(17)	7	0.5	0.6983(15)	2	0.6	0.6974(16)		
				0.0220	18	0.5	0.7194(16)	7	0.5	0.7179(14)	2	0.6	0.7171(15)		
cC211.20.48	205	13	34	0.0150	17	0.7	0.5906(30)	6	0.9	0.5888(30)	2	0.7	0.5863(32)	0.474(5)	7.76(19)
				0.0170	17	0.8	0.6062(28)	6	0.9	0.6043(28)	2	0.7	0.6021(29)		
cC211.06.80	401	16	39	0.0150	20	0.6	0.5766(14)	5	0.6	0.5759(10)	2	0.7	0.5756(12)	0.457(3)	7.93(1)
				0.0170	20	0.6	0.5926(12)	5	0.6	0.5919(9)	2	0.7	0.5917(11)		
				0.0190	20	0.7	0.6083(11)	5	0.6	0.6077(9)	2	0.7	0.6075(10)		

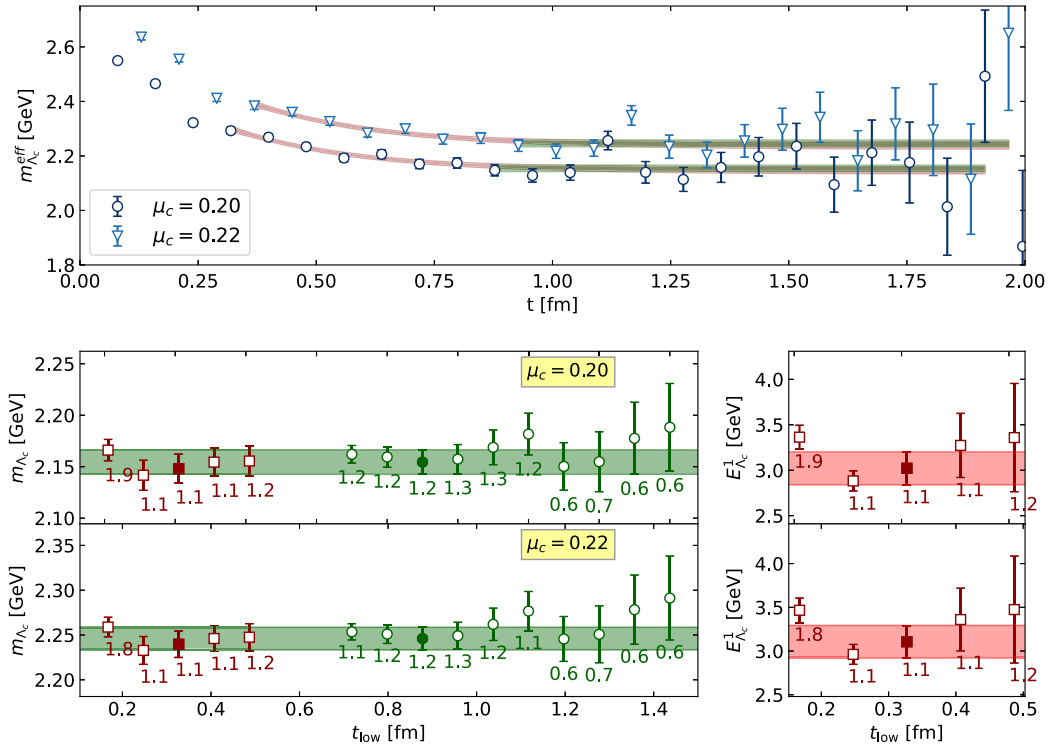


FIG. 14. The same as in Fig. 12 but for the case of Λ_c using the cB211.072.64 ensemble for the two values of μ_c given in the figure legend.

TABLE XVIII. The values of $m_{\Lambda_c}(\mu_c)$ mass, statistics used and fit parameters defined in Eq. (65) using a similar notation as that in Table XVII.

Ensemble	n_{conf}	n_{srcs}	t_{max}/a	$a\mu_c$	One-state fit			Two-state fit			aA_{Λ_c}	B_{Λ_c}/Z_P
					t_{low}/a	$\bar{\chi}^2$	am_{Λ_c}	t_{low}/a	$\bar{\chi}^2$	am_{Λ_c}		
cA211.30.32	287	16	22	0.21476	8	1.0	1.0200(26)	3	1.2	1.0180(32)	0.632(2)	1.807(11)
				0.26786	8	1.0	1.1177(29)	3	1.1	1.1153(39)		
				0.32214	8	0.9	1.2137(34)	3	1.0	1.2108(48)		
cA211.12.48	119	16	22	0.21476	8	1.0	1.0038(35)	1	0.2	1.0011(36)	0.619(4)	1.792(23)
				0.26786	8	0.8	1.1009(43)	1	0.3	1.0980(43)		
				0.32214	8	0.7	1.1957(52)	1	0.3	1.1925(52)		
cB211.25.32	360	16	26	0.17464	8	1.6	0.8554(18)	1	1.3	0.8542(17)	0.533(2)	1.8454(80)
				0.21830	8	1.5	0.9375(20)	1	1.2	0.9362(18)		
				0.26196	8	1.4	1.0163(22)	1	1.2	1.0148(20)		
cB211.25.48	649	16	31	0.17464	9	1.3	0.8506(12)	1	1.2	0.8504(10)	0.527(1)	1.8520(58)
				0.21830	9	1.2	0.9331(13)	1	1.1	0.9327(12)		
				0.26196	9	1.2	1.0121(15)	1	1.1	1.0115(13)		
cB211.14.64	232	8	27	0.20000	9	1.0	0.8932(25)	2	1.2	0.8912(24)	0.519(2)	1.870(12)
				0.22000	9	1.1	0.9306(26)	2	1.4	0.9284(25)		
cB211.072.64	400	4	24	0.20000	11	1.2	0.8713(47)	4	1.1	0.8687(57)	0.501(4)	1.850(23)
				0.22000	11	1.2	0.9083(50)	4	1.1	0.9057(60)		
cC211.20.48	205	4	29	0.18000	13	0.8	0.7869(45)	4	0.6	0.7835(52)	0.455(4)	1.840(24)
				0.22000	13	0.8	0.8605(50)	4	0.6	0.8571(59)		
cC211.06.80	260	4	28	0.18000	12	0.9	0.7633(48)	3	0.7	0.7614(49)	0.434(4)	1.825(24)
				0.24000	12	1.0	0.8729(57)	3	0.8	0.8708(57)		

$$m_N(m_{ud}) = m_N^0 - 4c_1(2Bm_{ud}(1 + c_2a^2)) - \frac{3g_A^2}{16\pi f_\pi^2}(2Bm_{ud}(1 + c_2a^2))^{3/2}, \quad (63)$$

consistent to the order we are working and including $\mathcal{O}(a^2)$ effects both in the pion expansion in Eq. (63) with the coefficient c_2 and in the nucleon expansion in Eq. (5). We

thus have two fit parameters, B and c_2 , while the lattice spacings, m_N^0 and c_1 , are determined from Eqs. (5)–(7). The fit procedure is performed for the four values of the renormalization constant from Table VII, checking for consistency and estimating systematic effects in the determination of Z_P . Since the values we obtain using the different methods of extracting Z_P are in very good agreement, we average over them. The statistical error in

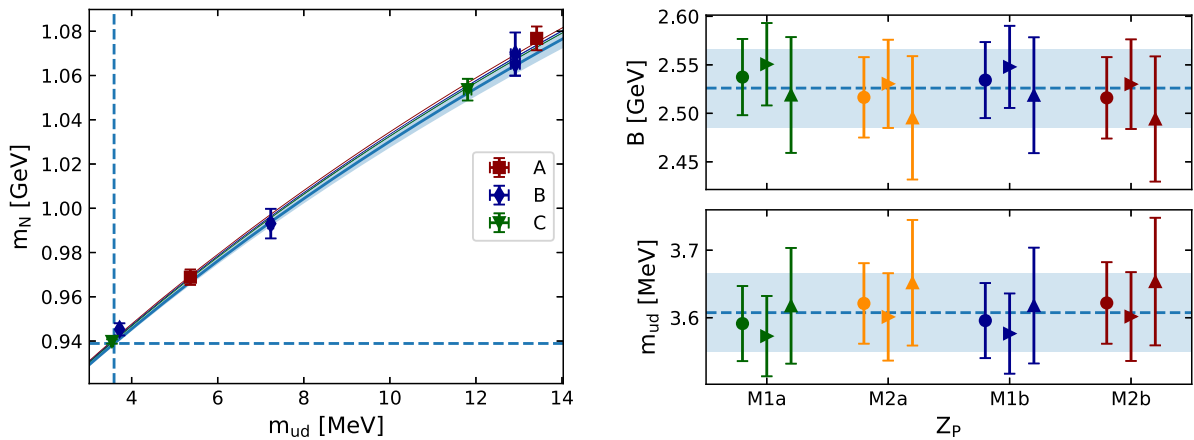


FIG. 15. Left panel: we show the nucleon mass m_N for the A (red), B (blue), and C (green) ensembles. The blue band shows the continuum extrapolation according to Eq. (63). Right panel: the values of the parameter B (top) and light quark mass (bottom) for different determinations of Z_P . Circles show the results using the mass of the nucleon from one-state fit in Table XVI. Right-pointing triangles show results when t_{low} is increased by one unit, namely, $t_{\text{low}}/a + 1$. Up-pointing triangles show results when the chiral extrapolation is done using ensembles with pion mass lower than 190 MeV. The dashed blue line is our final value obtained by the results listed in Table XIX.

TABLE XIX. Fit results for the extraction of the light quark mass with the nucleon mass using the four different estimation of the renormalization constants. The fit parameters are B and c_2 . The light quark mass m_{ud} is obtained as $m_\pi^{\text{isoQCD}}/(2B)$. The values are given in the $\overline{\text{MS}}$ scheme at 2 GeV.

Z_P	$\tilde{\chi}^2$	B (GeV)	c_2 (GeV ²)	m_{ud} (MeV)
M1a	0.7	2.537(39)	0.155(98)	3.591(56)
M2a	0.7	2.516(41)	0.49(11)	3.621(60)
M1b	0.8	2.534(39)	0.154(98)	3.596(56)
M2b	0.7	2.516(42)	0.57(11)	3.622(60)

the lattice spacing is taken into account in the jackknife analysis. The fit results are reported in Table XIX and depicted in Fig. 15. The final value of the light quark mass using the nucleon and pion mass, given in the $\overline{\text{MS}}$ scheme at 2 GeV, is

$$m_{ud} = 3.608(58)_{-19}^{+32} \text{ MeV}, \quad (64)$$

obtained by averaging the values in Table XIX. The systematic error is computed as in Eq. (42), but in the sum, we only take into account the mean values not included in the computation of the average. Namely, the systematic error reflects the choice of the fitting range estimated by increasing t_{low} by one unit and the sensitivity due to the chiral extrapolation estimated by using ensembles with pion mass smaller than 190 MeV. We will follow this procedure also for the computation of the systematic errors also for the strange and charm quark masses.

C. Strange and charm quark masses

We determine the strange and charm quark masses using the experimental value of the $\Omega(sss)$ and $\Lambda_c(udc)$ masses and the lattice spacings determined from the nucleon mass. Namely, we use $m_\Omega^{(\text{phys.})} = 1672.5(3)$ and $m_{\Lambda_c}^{(\text{phys.})} = 2286.5(1)$ from the particle data group (PDG) [36]. We use the renormalization constants Z_P given in Table VII.

We parametrize the Ω^- and Λ_c mass dependence on the strange and charm quark mass by expanding around \tilde{m}_s and \tilde{m}_c , that we chose to be in the same ballpark of the physical quark masses. In particular, we use $\tilde{m}_s = 95$ MeV and $\tilde{m}_c = 1.2$ GeV, and we interpolate around these reference points using

$$m_\Omega = A_\Omega + B_\Omega(m_s - \tilde{m}_s), \quad (65)$$

$$m_{\Lambda_c} = A_{\Lambda_c} + B_{\Lambda_c}(m_c - \tilde{m}_c). \quad (66)$$

We first discuss our procedure for the determination of the strange quark mass from the Ω mass. We then apply the same procedure for determining m_c using the Λ_c mass.

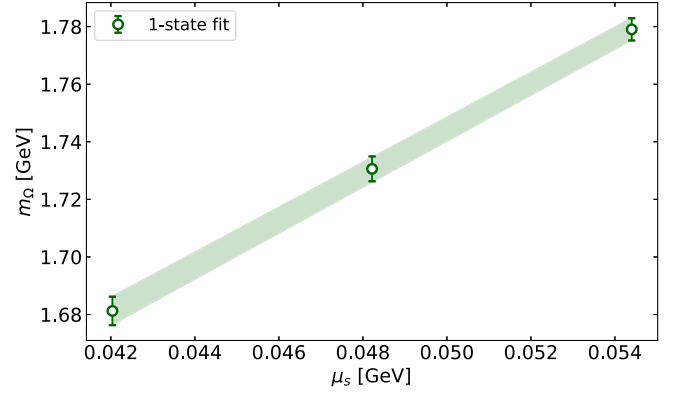


FIG. 16. Dependence of m_Ω on the μ_s bare quark mass for the cB211.072.64 ensemble. Data from the 1-state are reported, together with the linear extrapolation.

1. Strange quark mass

The knowledge of the Ω^- mass at three values of the valence strange quark mass parameter μ_s allows us to determine the Ω mass as a function of μ_s using the linear Ansatz of Eq. (65). We show a representative example of the resulting fit in Fig. 16 for the ensemble cB211.072.64. The same analysis is carried out for all the ensembles listed in Table XVII, where we give the values of A_Ω and B_Ω , defined in Eq. (65).

We employ two methods to determine m_s : In method I, we perform a chiral and continuum extrapolation of the A_Ω and B_Ω parameters separately. Namely, we expand to leading order in ChPT and include $\mathcal{O}(a^2)$ cutoff effects as follows,

$$A_\Omega(a, m_\pi^2) = c_1 + c_2 m_\pi^2 + c_3 a^2, \quad (67)$$

$$B_\Omega(a, m_\pi^2) = c'_1 + c'_2 m_\pi^2 + c'_3 a^2, \quad (68)$$

and we limit ourselves to ensembles with $m_\pi < 260$ MeV so that these leading-order expression are reliable.

In Fig. 17, we illustrate the chiral and continuum extrapolation for the parameters A_Ω and B_Ω using the value of Z_P from method M1a (see Table VII). We note that the values of A_Ω and B_Ω using the cB211.025.32 and cB211.025.48 ensembles are compatible, demonstrating that finite size effects are small. Using the values of the parameters A_Ω and B_Ω at the physical pion mass and continuum limit, we can extract the strange quark mass in the continuum limit and at the physical pion mass from

$$m_s = \tilde{m}_s + \frac{m_\Omega^{(\text{phys.})} - A_\Omega(0, m_\pi^{(\text{phys.})})}{B_\Omega(0, m_\pi^{(\text{phys.})})}. \quad (69)$$

In method II, we adopt an iterative strategy: namely, we start by fixing a value of the renormalized strange quark

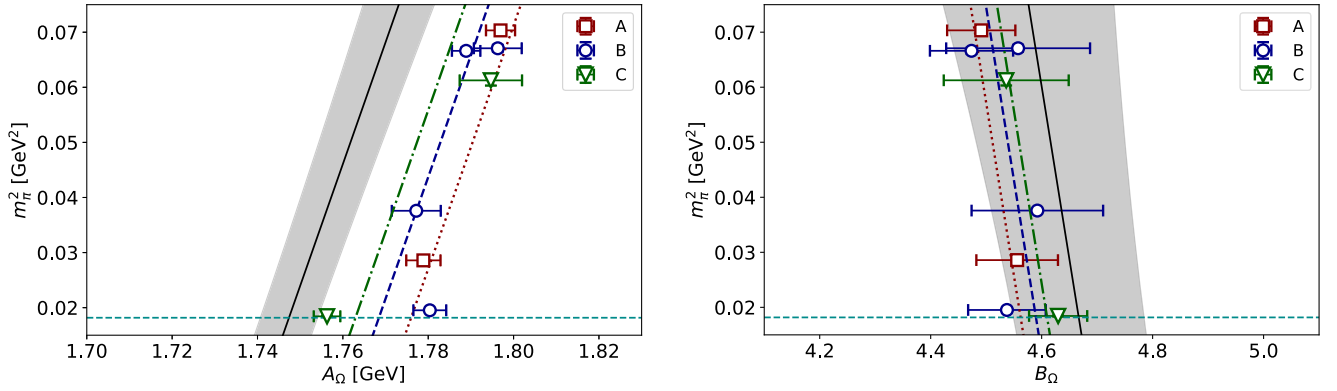


FIG. 17. Continuum and chiral extrapolation for the Ω^- in order to determine the coefficients of Eqs. (67) and (68). We show the pion mass squared as a function of A_Ω (left) and B_Ω (right) for the A (red), B (blue), and C (green) ensembles. The gray bands show the continuum extrapolation.

mass m_s in physical units for all the ensembles. We use Eq. (65) to interpolate to the given m_s . We then extrapolate to the continuum limit and physical point using the ChPT result

$$m_\Omega = m_\Omega^{(0)} - 4c_\Omega^{(1)} m_\pi^2 + d_\Omega^{(2)} a^2. \quad (70)$$

We iterate this procedure changing the value of m_s until the resulting value of m_Ω given in Eq. (70) at the physical point and continuum limit matches the physical value $m_\Omega^{(\text{phys})}$. In Fig. 18, we illustrate the analysis.

The results for the renormalized strange quark mass in the $\overline{\text{MS}}$ scheme at 2 GeV are provided in Table XX using the values of Z_P given in Table VII. We compare the different values by plotting them in Fig. 19. As can be seen,

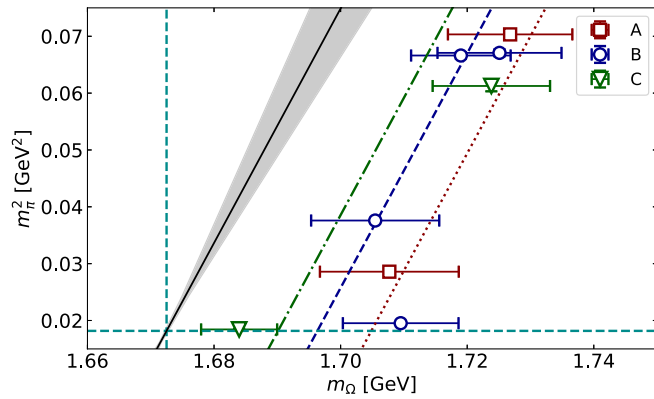


FIG. 18. We show the mass of the Ω^- , m_Ω at different pion mass squared for $m_s = 94.6(20)$ MeV, set by reproducing the physical mass of the Ω at the continuum limit as described in method II. The dotted lines show the chiral extrapolation for the A (red), B (blue), and C (green) ensembles. The solid black line shows the continuum extrapolation using Eq. (70) with the associated error (gray band). The horizontal and vertical dashed light blue lines represent, respectively, the physical pion and Ω masses.

despite the different values of Z_P at finite lattice spacing, in the continuum limit, we obtain very good agreement among different estimates of m_s . A similar agreement is also obtained between methods I and II discussed in this section for the determination of m_s . Since the error on the lattice spacing cannot be taken into account in a jackknife analysis because we used different statistics, we estimate the change in the value of m_s by varying the lattice spacing by a standard deviation. As can be seen in Fig. 19, this gives a

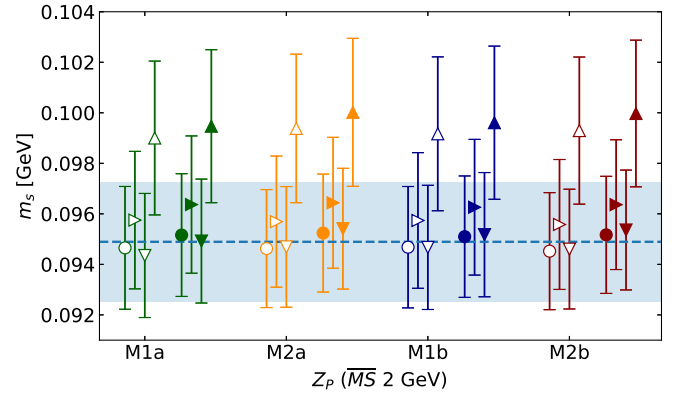


FIG. 19. The renormalized strange quark mass for different values of Z_P in the $\overline{\text{MS}}$ at 2 GeV. Symbols in green are obtained using method M1a, in orange are obtained using method M2a, in blue are obtained using method M1b, and in red are obtained using method M2b. For each value of Z_P , we give with open symbols the determination using method I to extract m_s and with filled symbols using method II. Circles show the results using the mass of the Ω from the one-state fit given in Table XVII. Triangles quantify systematic errors due to the selection of t_{low} (right-pointing triangles when $t_{\text{low}}/a + 1$), errors on the lattice spacing (down-pointing triangles increasing by a standard deviation the lattice spacings set by the nucleon mass), and errors due to chiral extrapolation (up-pointing triangles obtained using only ensembles with $m_\pi < 190$ MeV). The dashed line is the average over the values from method I and II and at different Z_P given in Tables XX and XXI.

TABLE XX. Results using method I and different values of Z_P as denoted in the first column. The second, third, fourth, and fifth columns give the reduced χ^2 of the fit to Eq. (67) and the values of the fit parameters c_1 , c_2 , and c_3 , respectively, that determine A_Ω in the continuum and chiral limit. The sixth, seventh, eighth, and ninth columns give the corresponding values for B_Ω of Eq. (68). In the last column, we give the extracted values for m_s in the $\overline{\text{MS}}$ scheme at 2 GeV.

Z_P	A_Ω				B_Ω				$\overline{\text{MS}}$ (2 GeV)
	$\bar{\chi}$	c_1 (GeV)	c_2 (GeV $^{-2}$)	c_3 (GeV fm $^{-2}$)	$\bar{\chi}'$	c'_1	c'_2 (GeV $^{-2}$)	c'_3 (fm $^{-2}$)	
M1a	3.7	1.739(7)	0.45(7)	3.3(1.1)	0.2	4.69(11)	-1.5(1.3)	-12(19)	94.6(2.5)
M2a	4.4	1.739(6)	0.44(6)	5.45(97)	0.2	4.67(12)	-1.6(1.4)	23(20)	94.6(2.3)
M1b	3.2	1.739(6)	0.44(7)	2.3(1.0)	0.3	4.68(11)	-1.6(1.3)	-10(19)	94.6(2.4)
M2b	4.6	1.739(6)	0.44(6)	6.19(96)	0.2	4.67(12)	-1.6(1.4)	31(20)	94.5(2.3)

TABLE XXI. Results using method II and different values of Z_P as denoted in the first column. In the second column, we give the reduced χ^2 of the fit, and in columns three, four, and five, we give the fit parameters of Eq. (70). In the last column, we give the extracted values for m_s in the $\overline{\text{MS}}$ scheme at 2 GeV.

Z_P	$\bar{\chi}$	$m_\Omega^{(0)}$ (GeV)	$c_\Omega^{(1)}$ (GeV $^{-1}$)	$d_\Omega^{(2)}$ (GeV fm $^{-2}$)	$\overline{\text{MS}}$ (2 GeV)
M1a	2.4	1.6636(16)	-0.121(21)	3.7(1.3)	95.1(2.5)
M2a	2.7	1.6637(15)	-0.120(20)	5.3(1.2)	95.2(2.3)
M1b	2.2	1.6638(15)	-0.118(21)	2.6(1.2)	95.0(2.4)
M2b	2.7	1.6637(15)	-0.120(20)	6.0(1.2)	95.1(2.3)

very small change compared to the statistical error. By increasing t_{low} of the one-state fit by one lattice unit gives an estimate of the systematic error in the extraction of the mass of the Ω . The change in the value of m_s is well within the statistical error, as can be seen in Fig. 19. We, thus, average over all the values obtained using the four different determinations of Z_P and analysis methods I and II (values are given in Tables XX and Table XXI). The systematic error is computed according to Eq. (42) but excluding the values over which we average. As for the case of μ_{ud} , the systematic error reflects systematics due to the choice of the fitting range by letting $t_{\text{low}}/a \rightarrow t_{\text{low}}/a + 1$ and systematics due to the chiral extrapolation by using ensembles with $m_\pi < 190$ MeV. Since the error in the lattice spacing cannot be included in the jackknife analysis due to using different statistics for the Ω , we include an additional term in Eq. (42) computed as the difference in the mean when we

change the lattice spacing within its error. Using as input the Ω^- mass, we obtain for m_s in the $\overline{\text{MS}}$ scheme at 2 GeV and the ratio m_s/m_{ud} the values

$$m_s = 94.9(2.4)_{-1.0}^{+4.1} \text{ MeV}, \quad m_s/m_{ud} = 26.30(61)_{-33}^{+1.17}, \quad (71)$$

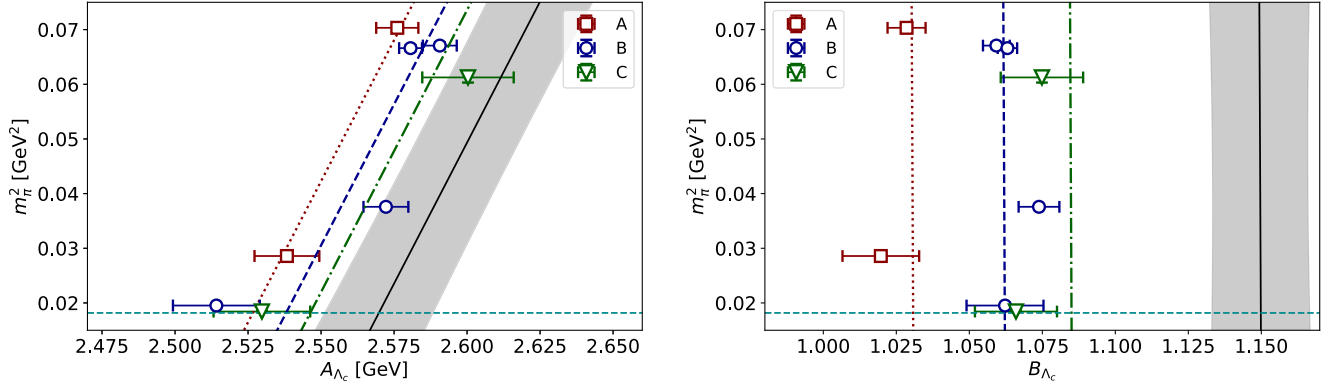
where for the ratio we use m_{ud} from Eq. (64). The error on the ratio is computed by combining in quadrature the errors on m_{ud} and m_s .

2. Charm quark mass

We employ the same procedure for the determination of m_c as described in the previous section for m_s using methods I and II. The mass of Λ_c is interpolated linearly in μ_c using Eq. (66) within the range spanned by the two μ_c

TABLE XXII. The same as in Table XX but for the A_{Λ_c} and B_{Λ_c} parameters. In the last two columns, the values for m_c in the $\overline{\text{MS}}$ scheme at 3 GeV are reported.

Z_P	A_{Λ_c}				B_{Λ_c}				$\overline{\text{MS}}$ (3 GeV)
	$\bar{\chi}$	c_1 (GeV)	c_2 (GeV $^{-1}$)	c_3 (GeV fm $^{-2}$)	$\bar{\chi}'$	c'_1	c'_2 (GeV $^{-2}$)	c'_3 (fm $^{-2}$)	
M1a	2.1	2.55(2)	0.9(2)	-4.9(2.6)	1.3	1.14(2)	0.00(15)	-13.7(2.5)	1030(21)
M2a	2.1	2.55(2)	0.9(2)	3.6(2.7)	1.6	1.15(2)	0.01(16)	-6.4(2.6)	1027(20)
M1b	2.2	2.54(2)	0.9(2)	-3.8(2.6)	1.0	1.14(2)	-0.03(15)	-12.8(2.5)	1037(21)
M2b	2.1	2.55(2)	1.0(2)	5.5(2.8)	1.7	1.15(2)	0.01(16)	-4.8(2.6)	1025(20)

FIG. 20. The same as for Fig. 17 but for the case of Λ_c .

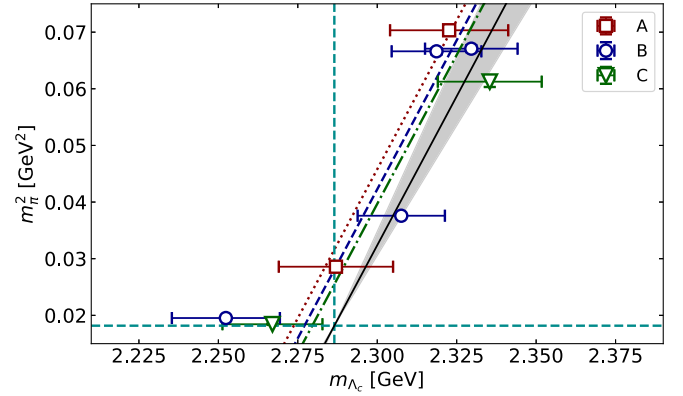
values. For the chiral extrapolation, we consider a similar expression to that used for Ω^- as given in Eq. (70), namely,

$$m_{\Lambda_c} = m_{\Lambda_c}^{(0)} + c_{\Lambda_c}^{(1)} m_\pi^2 + d_{\Lambda_c}^{(2)} a^2. \quad (72)$$

We note that to leading one loop in ChPT a m_π^3 -term with an unknown coefficient is present. Including such a term in the fit results in a coefficient consistent with zero and a $\chi^2/\text{d.o.f.} = 7.2$. That such a term is not supported by lattice QCD data was also found in our previous analysis using a larger set of pion masses [19] where this coefficient was found to be consistent with zero. We check that including it does not change the extracted value for m_c . Thus, given the larger χ^2 , we drop it from our analysis.

Results from method I are reported in Table XXII for all the values of Z_P listed in Table VII. We also illustrate in Fig. 20 the chiral and continuum extrapolations of A_{Λ_c} and B_{Λ_c} according to Eqs. (67) and (68), respectively, with Z_P determined using method M1a. The determination of the values of the parameters of Eq. (72) for method II is carried out as for the case of m_s , and the results are reported in Table XXIII and, for the M1a case, also in Figs. 21 and 22.

The values for m_c from methods I and II as well as how they change by varying the lattice spacings by a standard deviation and by the change in m_{Λ_c} by increasing t_{low} by one lattice spacing in the one-state fit are presented in Fig. 21.

FIG. 21. The same as for Fig. 18 but for the case of Λ_c .

Again, we observe a very good agreement between the results obtained via method I and method II and among different determinations of the Z_P renormalization constants. We thus average over these values and compute the systematic error in the same way as for μ_s . We obtain for the charm quark mass m_c in the $\overline{\text{MS}}$ scheme at 3 GeV and the ratio m_c/m_s the following values,

$$m_c = 1030(21)(^{+22}_{-5}) \text{ MeV}, \quad m_c/m_s = 12.05(31)(^{+58}_{-15}), \quad (73)$$

where the errors on the ratio are combined in quadrature.

TABLE XXIII. The same as in Table XXI but for the m_{Λ_c} extrapolation, according to Eq. (72). In the last column, we give the values for m_c in the $\overline{\text{MS}}$ scheme at 3 GeV.

Z_P	$\bar{\chi}$	$m_{\Lambda_c}^{(0)}$ (GeV)	$c_{\Lambda_c}^{(1)}$ (GeV $^{-1}$)	$d_{\Lambda_c}^{(2)}$ (GeV fm $^{-2}$)	$\overline{\text{MS}}$ (3 GeV)
					m_c (MeV)
M1a	2.7	2.2692(25)	0.95(14)	-1.4(2.0)	1030(21)
M2a	2.7	2.2689(26)	0.96(14)	5.3(2.2)	1026(20)
M1b	2.8	2.2695(25)	0.93(14)	-0.6(2.0)	1038(21)
M2b	2.7	2.2688(26)	0.97(15)	6.7(2.2)	1024(20)

TABLE XXIV. The renormalized quark masses determined in the meson sector (first row) and baryon sector (second row) in the $\overline{\text{MS}}$ scheme. In the third row, we give the average over the values obtained in the meson and baryon sectors, while in the last row, we give the latest FLAG averages [13] for $N_f = 2 + 1 + 1$. The light quark mass, m_{ud} (second column), and the strange quark mass, m_s (third column), are given at 2 GeV, while the charm quark mass, m_c (fourth column), is given at 3 GeV. The second error of the quark masses includes a 0.5% uncertainty (added in quadrature) due to the uncertainty of the conversion of the renormalization constants (RCs) Z_P to the $\overline{\text{MS}}$ scheme. In the fifth and sixth columns, we give the ratios m_s/m_{ud} and m_c/m_s , respectively. In the meson sector, the error on the ratio is determined in a jackknife analysis. In the baryon sector, since different ensembles are involved in the determination of the quark masses, the error on the ratio is propagated quadratically using the errors on each of the quark masses.

	m_{ud} (MeV)	m_s (MeV)	m_c (MeV)	m_s/m_{ud}	m_c/m_s
Meson sector	3.689(80)(66)	101.0(1.9)(1.4)	1039(15)(8)	27.30(24)(14)	11.43(9)(10)
Baryon sector	3.608(58)($^{+32}_{-19}$)	94.9(2.4)($^{+4.1}_{-1.0}$)	1030(21)($^{+22}_{-5}$)	26.30(61)($^{+1.17}_{-0.33}$)	12.04(31)($^{+58}_{-15}$)
Average	3.636(66)($^{+60}_{-57}$)	98.7(2.4)($^{+4.0}_{-3.2}$)	1036(17)($^{+15}_{-8}$)	27.17(32)($^{+56}_{-38}$)	11.48(12)($^{+25}_{-19}$)
FLAG 2019	3.410(43)	93.44(68)	988(7)	27.23(10)	11.82(16)

VII. CONCLUSIONS

The focus of this work is the determination of the light, strange, and charm quark masses. We perform an analysis of ten $N_f = 2 + 1 + 1$ ensembles simulated at three lattice spacings smaller than 0.1 fm and pion masses in the range from about 350 to 135 MeV. Having two ensembles simulated with the physical value of the pion mass at the two smallest lattice spacings enables us to extrapolate reliably to the physical and continuum limit.

The extraction of the quark masses is done using observables from both the meson sector and the baryon sector. The isosymmetric values of the pion, kaon, and D -meson masses as well as of the pion decay constant are used for the determination of the lattice spacings and the quark masses in the meson analysis. In the baryon sector, we use as inputs the nucleon and pion masses to obtain the lattice spacing and the average light-quark mass, while the masses of the Ω^- and Λ_c baryons determine the strange and charm quark masses.

In Table XXIV, we collect the values of the quark masses obtained in Secs. V and VI for the light and strange quark masses in the $\overline{\text{MS}}$ scheme at 2 GeV and for the charm quark mass at 3 GeV. Since the isospin and electromagnetic corrections to the nucleon mass are only known for the mass difference between the neutron and proton [37], in our analysis, we average over the mass of the proton and neutron. This defines a QCD prescription different from that used in the meson sector. Using the values of the lattice spacing extracted in the meson sector, we obtain a nucleon mass in the continuum limit a few MeV smaller than the input value $m_{N,phys} = 0.9389$ GeV adopted in the baryon sector (see Sec. III). This results in less than a percent change in the values given in the Table XXIV, which is much smaller than our statistical errors. It is thus justifiable to average over the values obtained in the meson and baryon sectors to produce our final values.

In order to perform the above average, we adopt the weighted approach given in Eqs. (40)–(42). We assume the following weights,

$$w_M \propto 1/(\sigma_M^{\text{stat}})^2, \quad w_B \propto 1/(\sigma_B^{\text{stat}})^2, \quad (74)$$

for the quantities coming from the mesonic and the baryonic sectors, where $\sigma_{M(B)}^{\text{stat}}$ is the first error given in the corresponding rows of Table XXIV. In this way, we obtain

$$\bar{x} \pm \sigma^{\text{stat}} \left(\begin{smallmatrix} +\sigma^{\text{stat},+} \\ -\sigma^{\text{stat},-} \end{smallmatrix} \right), \quad (75)$$

where

$$\bar{x} = w_M x_M + w_B x_B, \quad (76)$$

$$(\sigma^{\text{stat}})^2 = w_M (\sigma_M^{\text{stat}})^2 + w_B (\sigma_B^{\text{stat}})^2, \quad (77)$$

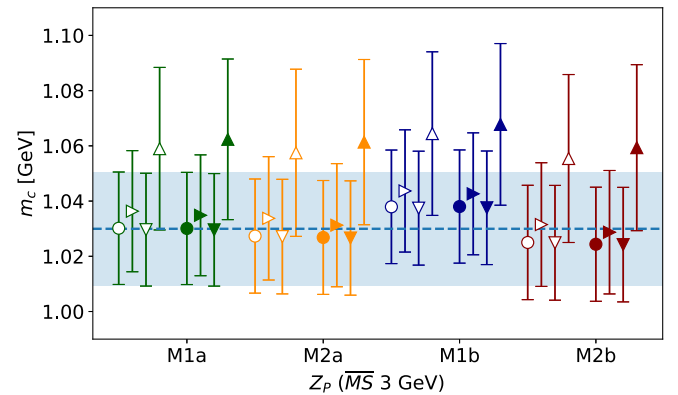


FIG. 22. We show the values of m_c for different determinations of Z_P and for methods I and II. The notation is the same as that of Fig. 19.

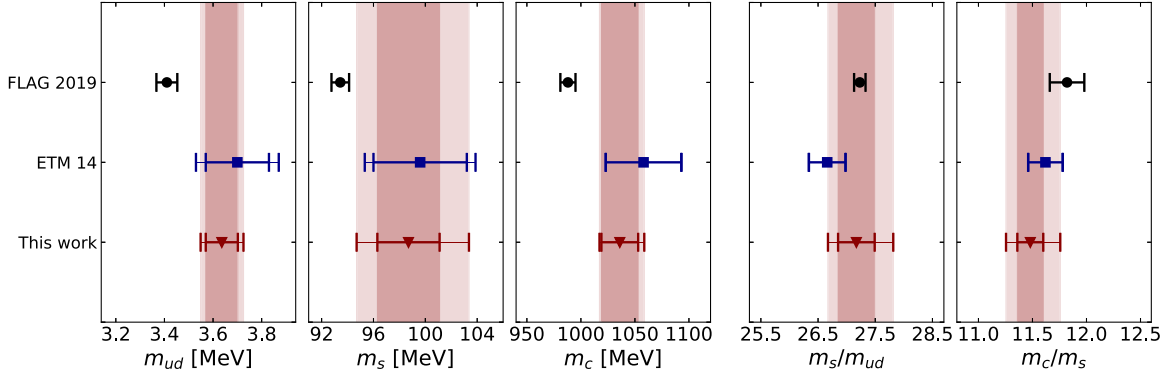


FIG. 23. Comparison of the results average between the values determined in the meson and baryon sectors (red triangles) with the values obtained using twisted-mass fermions in Ref. [12] (blue squares) and the $N_f = 2 + 1 + 1$ averages given in the last FLAG report [13] (black circles). The shorter error bars take into account the statistical error only, while the larger represent the total error, obtained by summing in quadrature the statistical and the systematic errors.

$$(\sigma^{\text{syst},\pm})^2 = w_M[(x_M - \bar{x})^2 + (\sigma_M^{\text{syst}})^2] + w_B[(x_B - \bar{x})^2 + (\sigma_B^{\text{syst},\pm})^2]. \quad (78)$$

The results are given in the last row of Table XXIV and are compared in Fig. 23 with those of the ETM analysis of Ref. [12] and the ones entering the $N_f = 2 + 1 + 1$ averages in the latest FLAG report [13]. The latter ones are based on the results of Refs. [12,38] for the light-quark mass, Refs. [12,38–40] for the strange mass, Refs. [12,19,38–40] for the charm mass, Refs. [12,41,42] for the m_s/m_{ud} ratio, and Refs. [12,38,40] for the m_c/m_s ratio.

It can be seen that our results are larger by approximately 2.5 standard deviations in the case of m_{ud} and by approximately 2 standard deviations in the case of m_c with respect to the corresponding FLAG values. Although for the strange quark mass our result coming from the meson sector is larger by approximately 3 standard deviations, our averaged result is consistent with the FLAG one within our final uncertainty. Good agreement is observed for the mass ratios m_s/m_{ud} and m_c/m_s . We do not believe that these differences can be ascribed to possible uncontrolled effects on the mass renormalization constant $1/Z_P$. Indeed, the detailed analysis carried out in this work concerning the pion pole subtraction and the residual hadronic contaminations in the RI-MOM determination of the renormalization constant Z_P leaves little room for any significant leftover contribution from these terms. Our findings point to the fact that hadronic contaminations are controlled at the level of few per mille. Therefore, we do not consider it plausible that the observed tension with the FLAG values may be related to uncontrolled hadronic contaminations on the mass renormalization constant. In this respect, we are considering the possibility of repeating the determination of the quark masses using the same extended twisted mass (ETM) gauge ensembles adopted in this work, but evaluating the mass renormalization in a different scheme, like

RI-SMOM, while keeping the same level of control of the hadronic contaminations achieved in this work.

Our final results for the light, strange, and charm quark masses as well for the mass ratios m_s/m_{ud} and m_c/m_s are consistent with our previous analysis of Ref. [12] (see also Fig. 23), which was based on Wilson twisted-mass fermions far from the physical pion point. The overall uncertainties for the light and charm quark masses are reduced by a factor of approximately 1.7–2.0, while in the case of the strange quark mass, the uncertainty is almost unchanged, partly due to the difference between the mean values obtained in the meson and baryon sector, which is added to the systematic error. This is also reflected in the two ratios. With respect to the quark mass analysis of Ref. [12], the main improvements are (i) a better control of the chiral extrapolation thanks to gauge ensembles produced close to the physical pion point; (ii) a better control of hadronic contaminations in the calculations of the mass renormalization constant; and (iii) the use of both mesonic and baryonic quantities, which requires simulations of different correlation functions. For all the three masses, the contribution from lattice systematics is important, in particular in the case of m_s . Our plan is to add at least one further gauge ensemble at a fourth finer value of the lattice spacing at the physical point. This will allow a tightly controlled chiral and continuum extrapolations in both the meson and baryon sectors.

ACKNOWLEDGMENTS

We would like to thank all members of ETMC for a very constructive and enjoyable collaboration. We acknowledge Partnership for Advanced Computing in Europe (PRACE) for awarding us access to the high-performance computing system Marconi and Marconi100 at Consorzio Interuniversitario per il Calcolo Automatico dell’Italia Nord-orientale under the Grants No. Pra17-4394, No. Pra20-5171, and No. Pra22-5171 and CINECA for

providing us CPU time under the specific initiative INFN-LQCD123. We also acknowledge PRACE for awarding us access to HAWK, hosted by HLRS, Germany, under the grant with Acid 33037. The authors gratefully acknowledge the Gauss Centre for Supercomputing e.V. (www.gauss-centre.eu) for funding the project pr74yo by providing computing time on the GCS Supercomputer SuperMUC at Leibniz Supercomputing Centre (www.lrz.de); the projects ECY00, HCH02, and HBN28 on the GCS supercomputers JUWELS and JUWELS Booster [43] at the Jülich Supercomputing Centre (JSC); and time granted by the John von Neumann Institute for Computing on the supercomputers JURECA and JURECA Booster [44], also at JSC. Part of the results were created within the EA program of JUWELS Booster also with the help of the JUWELS Booster Project Team (JSC, Atos, ParTec, NVIDIA). We further acknowledge computing time granted on Piz Daint at Centro Svizzero di Calcolo Scientifico via Project No. s702. Part of the statistics of the cA211.30.32 ensemble used in this work was generated on the Bonna cluster at the University of Bonn, access to which the authors gratefully acknowledge. This work has been partially supported by the Horizon 2020 research and innovation program of the European Commission under the Marie Skłodowska-Curie Grant No. 765048 (STIMULATE) as well as by the DFG as a

project under the Sino-German CRC110. R. F. acknowledges the University of Rome Tor Vergata for the support granted to the project PLNUGAMMA. F. S. and S. S. are supported by the Italian Ministry of Research under Grant No. PRIN 20172LNEEZ. F. S. is supported by INFN under GRANT73/CALAT. P. D. and E. F. acknowledge support from the European Unions Horizon 2020 research and innovation programme under the Marie Skłodowska-Curie Grant No. 813942 (EuroPLEX). P. D. acknowledges support from INFN under the research project INFN-QCDLAT. M. C. acknowledges financial support by the U.S. Department of Energy, Office of Nuclear Physics Early Career Award under Grant No. DE-SC0020405. S. B. and J. F. are supported by the H2020 project PRACE 6-IP (Grant No. 82376) and the EuroCC project (Grant No. 951740). F. M. and A. T. are supported by the European Joint Doctorate program STIMULATE Grant No. 765048. K. H. and E. P. are supported by the Cyprus Research and Innovation Foundation under Contract No. POST-DOC/0718/0100. F. P. acknowledges support from project NextQCD, cofunded by the European Regional Development Fund and the Republic of Cyprus through the Research and Innovation Foundation (EXCELLENCE/0918/0129). M. D. C. is supported in part by UK STFC Grant No. ST/P000630/1.

-
- [1] R. Frezzotti, P. A. Grassi, S. Sint, and P. Weisz (Alpha Collaboration), *J. High Energy Phys.* **08** (2001) 058.
 - [2] B. Sheikholeslami and R. Wohlert, *Nucl. Phys.* **B259**, 572 (1985).
 - [3] R. Baron *et al.*, *J. High Energy Phys.* **06** (2010) 111.
 - [4] R. Frezzotti and G. C. Rossi, *J. High Energy Phys.* **08** (2004) 007.
 - [5] R. Frezzotti and G. C. Rossi, *J. High Energy Phys.* **10** (2004) 070.
 - [6] M. Constantinou *et al.* (ETM Collaboration), *J. High Energy Phys.* **08** (2010) 068.
 - [7] R. Frezzotti, G. Martinelli, M. Papinutto, and G. C. Rossi, *J. High Energy Phys.* **04** (2006) 038.
 - [8] P. Boucaud *et al.* (ETM Collaboration), *Comput. Phys. Commun.* **179**, 695 (2008).
 - [9] A. Abdel-Rehim *et al.* (ETM Collaboration), *Phys. Rev. D* **95**, 094515 (2017).
 - [10] C. Alexandrou *et al.*, *Phys. Rev. D* **98**, 054518 (2018).
 - [11] C. Alexandrou *et al.*, [arXiv:2104.06747](https://arxiv.org/abs/2104.06747).
 - [12] N. Carrasco *et al.* (European Twisted Mass Collaboration), *Nucl. Phys.* **B887**, 19 (2014).
 - [13] S. Aoki *et al.* (Flavour Lattice Averaging Group), *Eur. Phys. J. C* **80**, 113 (2020).
 - [14] R. Frezzotti and G. C. Rossi, *Nucl. Phys. B, Proc. Suppl.* **128**, 193 (2004).
 - [15] R. Baron *et al.* (European Twisted Mass Collaboration), *Comput. Phys. Commun.* **182**, 299 (2011).
 - [16] K. Osterwalder and E. Seiler, *Ann. Phys. (N.Y.)* **110**, 440 (1978).
 - [17] S. Aoki *et al.*, *Eur. Phys. J. C* **77**, 112 (2017).
 - [18] C. Alexandrou and C. Kallidonis, *Phys. Rev. D* **96**, 034511 (2017).
 - [19] C. Alexandrou, V. Drach, K. Jansen, C. Kallidonis, and G. Koutsou, *Phys. Rev. D* **90**, 074501 (2014).
 - [20] J. Gasser, M. E. Sainio, and A. Svarc, *Nucl. Phys.* **B307**, 779 (1988).
 - [21] B. C. Tiburzi and A. Walker-Loud, *Phys. Lett. B* **669**, 246 (2008).
 - [22] B. Märkisch *et al.*, *Phys. Rev. Lett.* **122**, 242501 (2019).
 - [23] G. Martinelli, C. Pittori, C. T. Sachrajda, M. Testa, and A. Vladikas, *Nucl. Phys.* **B445**, 81 (1995).
 - [24] M. Constantinou, R. Horsley, H. Panagopoulos, H. Perlt, P. E. L. Rakow, G. Schierholz, A. Schiller, and J. M. Zanotti, *Phys. Rev. D* **91**, 014502 (2015).
 - [25] C. Alexandrou, M. Constantinou, and H. Panagopoulos (ETM Collaboration), *Phys. Rev. D* **95**, 034505 (2017).
 - [26] K. G. Chetyrkin and A. Retey, *Nucl. Phys.* **B583**, 3 (2000).
 - [27] S. R. Sharpe, *Phys. Rev. D* **56**, 7052 (1997); **62**, 099901(E) (2000).
 - [28] S. Borsanyi *et al.*, *J. High Energy Phys.* **09** (2012) 010.

- [29] M. Lüscher, *J. High Energy Phys.* **08** (2010) 071; **03** (2014) 092(E).
- [30] G. Bergner, P. Dimopoulos, J. Finkenrath, E. Fiorenza, R. Frezzotti, M. Garofalo, B. Kostrowa, F. Sanfilippo, S. Simula, and U. Wenger (Extended Twisted Mass Collaboration), *Proc. Sci. LATTICE2019* (**2020**) 181 [arXiv:2001.09116].
- [31] J. Gasser and H. Leutwyler, *Ann. Phys. (N.Y.)* **158**, 142 (1984).
- [32] B. Blossier, M. Della Morte, G. von Hippel, T. Mendes, and R. Sommer, *J. High Energy Phys.* **04** (2009) 094.
- [33] C. R. Allton *et al.* (UKQCD Collaboration), *Phys. Rev. D* **47**, 5128 (1993).
- [34] M. Falcioni, M. Paciello, G. Parisi, and B. Taglienti, *Nucl. Phys.* **B251**, 624 (1985).
- [35] O. Bar, *Phys. Rev. D* **92**, 074504 (2015).
- [36] P. D. Group, P. A. Zyla *et al.*, *Prog. Theor. Exp. Phys.* **2020**, 083C01 (2020).
- [37] S. Borsanyi *et al.*, *Science* **347**, 1452 (2015).
- [38] A. Bazavov *et al.* (Fermilab Lattice, MILC, TUMQCD Collaborations), *Phys. Rev. D* **98**, 054517 (2018).
- [39] A. T. Lytle, C. T. H. Davies, D. Hatton, G. P. Lepage, and C. Sturm (HPQCD Collaboration), *Phys. Rev. D* **98**, 014513 (2018).
- [40] B. Chakraborty, C. T. H. Davies, B. Galloway, P. Knecht, J. Koponen, G. C. Donald, R. J. Dowdall, G. P. Lepage, and C. McNeile, *Phys. Rev. D* **91**, 054508 (2015).
- [41] A. Bazavov *et al.* (Fermilab Lattice, MILC Collaborations), *Phys. Rev. D* **90**, 074509 (2014).
- [42] A. Bazavov *et al.*, *Phys. Rev. D* **98**, 074512 (2018).
- [43] Jülich Supercomputing Centre, *J. Large-Scale Res. Facil.* **5**, A135 (2019).
- [44] Jülich Supercomputing Centre, *J. Large-Scale Res. Facil.* **4** (2018).